Doctoral Dissertation (Censored)
博士論文 （要約）

Structure and behaviour of pure and salty ice VII from *in-situ* neutron diffraction techniques with development of high-pressure cells

(高圧セル開発とその場中性子回折による
純粋および塩を含む氷 VII 相の構造と挙動)

A Dissertation Submitted for the Degree of Doctor of Philosophy
December 2021
令和 3 年 12 月博士（理学）申請

Department of Chemistry, Graduate School of Science,
The University of Tokyo
東京大学大学院理学系研究科
化学専攻

Keishiro Yamashita
山下 恵史朗

Abstract

Water is a ubiquitous material and also one of the simplest molecules. In spite of its simplicity as a molecule, water has a structural variety in condensed phases. Water molecules are regarded as a tetrahedrally building unit in ice structures. Ice VII is a crystalline phase of water and stable above 2 GPa at room temperature. Its structure can be expressed by a highly symmetric cubic model called the "single-site" model (Figure 1). The orientations of water molecules are disordered in ice VII, but they become ordered in ice VIII at low temperature retaining the topology of the hydrogen bonding network. Ice VII exhibits unique behaviours such as cross-over of proton dynamics at 10 GPa [1] and symmetrisation of hydrogen bonds towards ice X at 60 GPa [2]. Moreover, ice VII is reported to structurally incorporate ionic species in contrast to ordinary ice I [3–5]. Neutron diffraction is a strong technique to investigate the structures for their sensitivity to hydrogen (deuterium). In this thesis, I investigated the structures and thermodynamic behaviours of pure and salty ice VII from neutron diffraction experiments under high pressure.

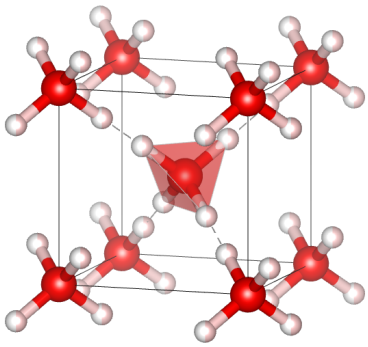

Figure 1: Single-site model of ice VII with tetrahedron describing coordination geometry of water molecule.

Chapter 2 describes developments of diamond anvil cells (DACs) for single-crystal neutron diffraction with their feasibility test on diffraction measurements. Single-crystal diffraction is the basis of diffraction techniques because it provides three-dimensional information, whereas powder diffraction inevitably reduces structural information into one dimension as a result of orientational averages of crystallites. However, single-crystal diffraction is still challenging for high-pressure experiments because neutron beams are blocked by bulky high-pressure vessels. I overcame this limitation by isolating the sample from a massive loading frame using special materials: nano-polycrystalline diamond (NPD) for anvils and Zr-based bulk metallic glass (BMG) for a cylinder [6] (Figure 2). Both NPD and Zr-BMG are highly neutron transparent so that neutron beams can travel through the DAC with sufficient intensity from/to arbitrary directions. Moreover, these materials do not

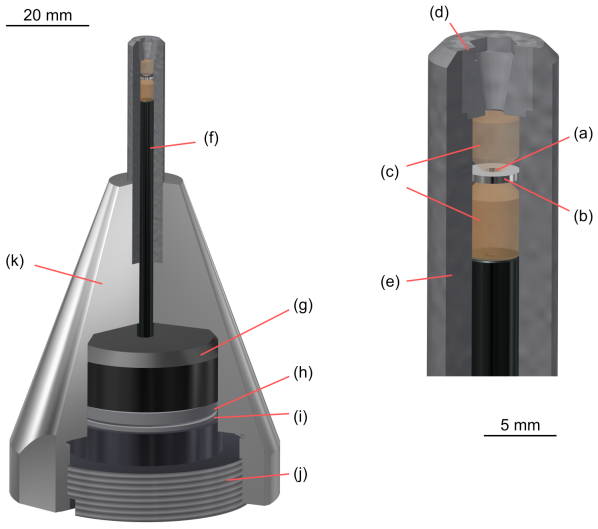

Figure 2: Schematic image of the developed DAC; (a) sample, (b) gasket, (c) anvils, (d) back nut, (e) cylinder, (f) piston tube, (g) piston, (h) bearing, (i) spacer, (j) back screw, and (k) body.

produce serious parasitic diffractions. Such extra diffraction from conventional materials such as alloys and single-crystalline diamonds are harmful to distinguish the signals from the sample.

The developed DAC was confirmed to stably generate 4.5 GPa, sufficient pressure for this study. For comparison with the conventional sample mounting, diffraction patterns were collected for NaCl and NH_4Cl at the D9 beamline of the Institut Laue-Langevin (ILL, France) and at the BL18 (SENJU) beamline of the Material and Life Science Experimental Facility (MLF) at J-PARC (Ibaraki, Japan), respectively. Both experiments resulted in plausible structure refinements with R-factors better than 10% with tiny crystals smaller than 0.1 mm^3. High-pressure diffraction measurements were also conducted for pure ice VI at *ca.* 1 GPa.

Chapter 3 describes detailed structure analyses of pure ice VII by the combination of single-crystal and powder neutron diffraction. The single-site model is adopted in many studies because of its simplicity and reproducibility of diffraction patterns. However, it gives an unrealistic molecular geometry in the structure refinement such as an unlikely short O-D covalent bond length of 0.89 Å quite shorter than that in ice VIII (0.97 Å) [7]. This is because the structure model, averaged in time and space, does not match the intrinsic atomic positions. Then structure models with multiple displaced sites have been proposed to describe the structure of ice VII with plausible molecular geometry [7, 8]. However, no unambiguous structure refinements have been achieved so far due to the small displacements to determine experimentally. In this study, neutron diffraction measurements were conducted on single crystals and powder samples using the developed DAC at the D9 and MITO system [9] at the BL11 (PLANET) beamline, MLF, J-PARC, respectively. Deuterated samples were used to avoid incoherent scattering.

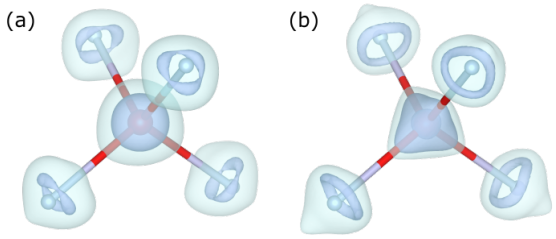

Figure 3: Distribution of scattering-length density in ice VII at 298 K and 2.2 GPa derived from (a) single crystal data and (b) powder diffraction data. The oxygen and deuterium are illustrated as those in the single-site model with O-D = 0.97 Å for comparison.

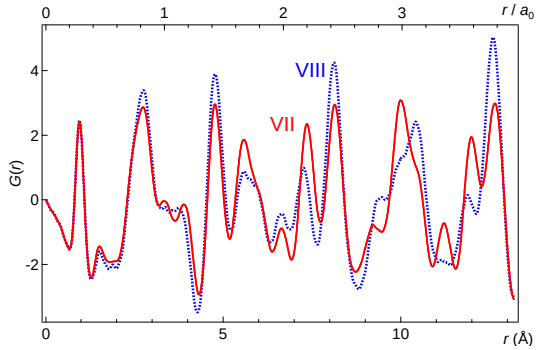

Figure 4: Pair distribution functions $G(r)$ of ice VII (red solid line) and VIII (blue dotted line) obtained at 274 K and 2.2 GPa. The top abscissa is normalised interatomic distance by the length of an edge of the unit-cell of ice VII a_0 = 3.346 632 Å derived in the Rietveld analysis.

Three-dimensional atomic distributions were obtained by applying a maximum entropy method (MEM) to both diffraction data at 2.2 GPa and 298 K (Figure 3). The derived density distributions revealed unexpected ring-like distributions of deuterium around the average O-O axis as well as oxygen displacement along ⟨111⟩ directions. Those could not be clarified in previous diffraction studies.

The interatomic structures of ice VII and VIII were derived by a total scattering analysis of the powder diffraction data at 274 K and 2.2 GPa (Figure 4). Individual peak fitting gave the

O-D distance of 0.9662(5) Å in ice VII comparable to that in ice VIII as expected. Despite the similarity of the pair distribution function (PDF), $G(r)$, of ice VII and VIII at the short distances, they differed at longer distances than the size of the unit cell of ice VII ($\approx$ 3.3 Å). These findings indicate that molecular behaviours are actually identical between ice VII and VIII, but their intermolecular structure is distinct between them. The apparently short O-D distances in ice VII obtained by conventional structure analyses are caused by spatial and time averaging of the various molecular configurations in the disordered structure of ice VII.

Chapter 4 describes the behaviours of salty ice VII in its excess volumes and hydrogen disordering. Ice VII is known to structurally incorporate salt such as NaCl, LiCl, $MgCl_2$ [3–5], *etc.* in contrast to ordinary ice I_h. Salt-incorporated ice VII can be prepared in two ways. A path via amorphisation at low temperature before compression is the way for salty VII with high salinity up to 15 mol% [10]. The obtained salty ice VII has drastic volume expansion and disturbance of hydrogen ordering at low temperature. Compression at room temperature from liquid phase gives one with lower salinity than 2 mol% [3, 5]. There is a gap between these studies which cannot be explained in a simple doping description. I investigated the volume change and hydrogen ordering of salty ice VII by sequential measurements of neutron powder diffraction using the MITO system at the BL11 (PLANET).

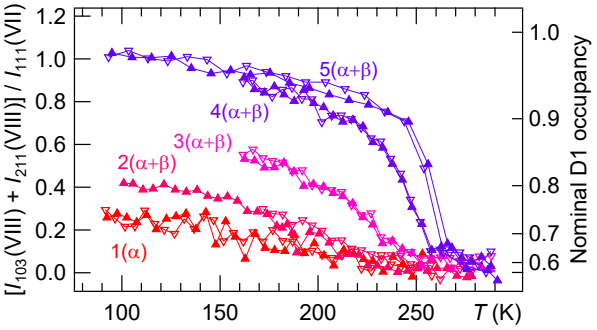

Figure 5: Temperature dependencies of hydrogen ordering features in path A. Summed diffraction intensities corresponding to 103 and 211 diffractions of ice VIII are normalised by that of 202 diffraction of ice VIII (111 of ice VII) at the highest temperature in each cycle. Downward open and upward filled triangles indicate cooling and heating procedures, respectively. The numbering of each plot correspond to annealing steps at 1) 265 K, 2) 285 K, 3) 315 K, 4) 340 K, and 5) 370 K. The right ordinate corresponds to nominal D1 occupancy calculated from a structure model of partially ordered ice VIII with cubic symmetry.

Salty ice VII was obtained starting from solutions of $MgCl_2$:D_2O = 1:25 (in molar) via saline amorphous at low temperature in two runs. A salty ice VII crystallised during heating at *ca.* 4 GPa in path A with the excess volumes over 5% compared to pure ice [11]. This large volume expansion was also observed in the other run. α-VII did not show features of hydrogen ordering (Figure 5) like the reported case of LiCl [4]. After further annealing at higher temperatures, the peaks of ice VII was broadened and split into two types of ice VII apparently. The other ice VII (hereafter β-VII) had smaller excess volumes and showed the increase of the hydrogen ordering features according to annealing. α-VII disappeared after further annealing while β-VII remained with volume decrease into 0%. Thus β-VII would be described by a simple doping model like as discussed in the salty ices obtained at ambient pressure compression [5]. The features of α-VII had a gap from β-VII suggest α-VII would be somewhat metastable with non-negligible potential minima. Although α-VII is energetically unfavoured at higher temperatures, it would be not simply a kinetically-trapped state like β-VII. It is not clear what is the main factor of

their differences, but the structural difference is considered to be the major factor considering the fact that diffraction peaks of salt hydrates became obvious after α-VII almost disappeared.

In conclusion, I clarified the detailed structure of pure ice VII by single-crystal neutron diffraction using the newly-developed DAC combined with powder diffraction. Ice VII has a distinct intermolecular structure from its ordered counterpart, ice VIII, but the molecular geometry is identical as expected empirically. The atomic distribution derived by the MEM analysis highlighted the insufficiency of the discrete structure models to describe the disordered structure of ice VII. From *in-situ* powder neutron diffraction, I proposed two types of salty ice VII crystallised from saline amorphous depending on further annealing. They are considered to qualitatively explain the previously reported salty ice VIIs. Moreover, crystallisation from amorphous phases is a long-standing issue in which kinetic factors compensate for thermodynamic stability at low temperatures. As supposed for pure ices (*e.g.* [12]), the crystalline phases and amorphous would have structural similarity. Further investigations with distinguishing α- and β-VII will be a new window for the comprehensive understanding of the ambiguous amorphous and salt-incorporated ice VII.

References

1. Yamane, R. *et al. Phys. Rev. B* **104,** 214304 (2021).
2. Lee, C. *et al. Phys. Rev. Lett.* **69,** 462–465 (1992).
3. Frank, M. R. *et al. Phys. Earth Planet. Inter.* **155,** 152–162 (2006).
4. Klotz, S. *et al. Nat. Mater.* **8,** 405–409 (2009).
5. Watanabe, M. *et al. Jpn. J. Appl. Phys.* **56,** 05FB03 (2017).
6. Yamashita, K. *et al. High Press. Res.* **40,** 88–95 (2020).
7. Kuhs, W. F. *et al. J. Chem. Phys.* **81,** 3612–3623 (1984).
8. Nelmes, R. J. *et al. Phys. Rev. Lett.* **81,** 2719–2722 (1998).
9. Komatsu, K. *et al. High Press. Res.* **33,** 208–213 (2013).
10. Klotz, S. *et al. Sci. Rep.* **6,** 32040 (2016).
11. Klotz, S. *et al. Phys. Rev. B* **95,** 174111 (2017).
12. Shephard, J. J. *et al. J. Phys. Chem. Lett.* **8,** 1645–1650 (2017).

Contents

1 General Introduction

The water molecule, denoted as H_2O, is a simple molecule consisting of one oxygen and two hydrogen atoms. Hydrogen atoms are covalently bonded to the oxygen, forming the bent H-O-H molecular structure. Despite the simplicity of the molecule, its condensed phases are not fully understood yet over the long years.

It should start from the atomic scale description before the complicated story. The molecular geometry of H_2O has been well studied from both experimental and theoretical approaches. The O-H covalent bond length is 0.96 Å and ∠HOH is 104.5° in vapour [1, 2]. High-level *ab initio* calculation predicted the possibility of their geometry changes in O-H distance of 0.930-0.989 Å and H-O-H angle of 96.4-112.8° within the energy colt below 4.184 J mol^{-1} [3]. In such an almost isolated condition, the water molecule does not interact with other molecules. On the other hand, water molecules interact with the neighbouring molecules in condensed phases. One of the characteristic interactions between water molecules is the hydrogen bond. The hydrogen bond is simply explained as a coulombic interaction induced by intrinsic polarisation between hydrogen and oxygen atoms. In detail, hydrogen bonds have somewhat covalent features with delocalisation of the molecular orbital [4–7]. The molecular orbital contributes to the electronic structure in the hydrogen bonds and the hydrogen bonds have features as directional bonds like covalent bonds in contrast to almost isotropic interaction of ionic or Van der Waals interactions. The energetic contribution of hydrogen bonds is smaller than the covalent bonds in each molecule but larger than the interatomic dipole-dipole interaction. Hydrogen bonds in the condensed phases slightly elongate the intramolecular O-H bonds to be 0.97–0.99 Å for liquid water [8, 9] and ordinary ice I [10, 11]. Such molecular structure is expected to not vary among the phases significantly [12].

The condensed phases of water can be distinguished by the arrangements of water molecules, *i.e.* the bonding structure among water molecules. Liquid phases are a common Highly-disordered phase in which the water molecules align almost randomly and move dynamically. When the motion of water molecules are frozen, water in such a condition can be called glassy liquid or amorphous ice. It is difficult to determine the exact positions of atoms and uniquely define the structures of condensed phases in a bulk size. Crystalline phases of ice have periodic structures in which atoms align in some arrangement orders. A structural unit and its periodicity can represent such structures. Diffraction experiments provide information on their periodicity and aperiodic units. In contrast to the crystalline phases, liquid and amorphous phases are non-periodic. The highly-disordered disordered structures are vague and difficult to characterise. This ambiguity leads the controversial discussions on the liquid-liquid critical point and the polyamorphism of water [13, 14].

1.1 Ice polymorphs in crystalline phases

Various experiments have found twenty polymorphs of crystalline ice up to now (Figure 1.1). These identified phases are numbered with Roman characters like I_h, I_c, II, ⋯ XIX. The structures of crystalline ice can be identified in many ways, *e.g.* by the crystal symmetry, and topological classification is useful to understand the hydrogen-bonding structures. In the classification, the hydrogen bond is regarded as a connection between oxygen atoms via one hydrogen. Then, the clustering water structure can be interpreted as networks consisting of hydrogen bonds and oxygen nodes. As a basic explanation, each water molecule can have four hydrogen bonds: two hydrogen bonds via its own hydrogen atoms and two via hydrogen atoms of the neighbours. These bonds are distinguished as hydrogen donation and acceptance, respectively. The four-coordinated water molecules behave as building blocks to construct the condensed phases like liquid, crystalline ice phases and amorphous ices forming the hydrogen-bonded network. Thus, water molecules are regarded as tetrahedral building units. The water molecules retain their tetrahedral coordinating features as two donors and two acceptors of hydrogen. Such coordinating restriction is known as the Bernal and Fowler's ice rules [15]. The structures of crystalline phases can be interpreted by these hydrogen-bonding networks. Ice I_h is the ordinary ice and forms from liquid water by cooling below 273 K. Ice I_c is a metastable phase and exists at lower temperatures. It has a similar structure with ice I_h except for layer stacking [16–18] with the same network topology with diamond. These stacking can mix with the other and such ice with disorder of layer stacking is called ice I_{sd} [19–21]. The subscripts on their numbering mean hexagonal, cubic, and

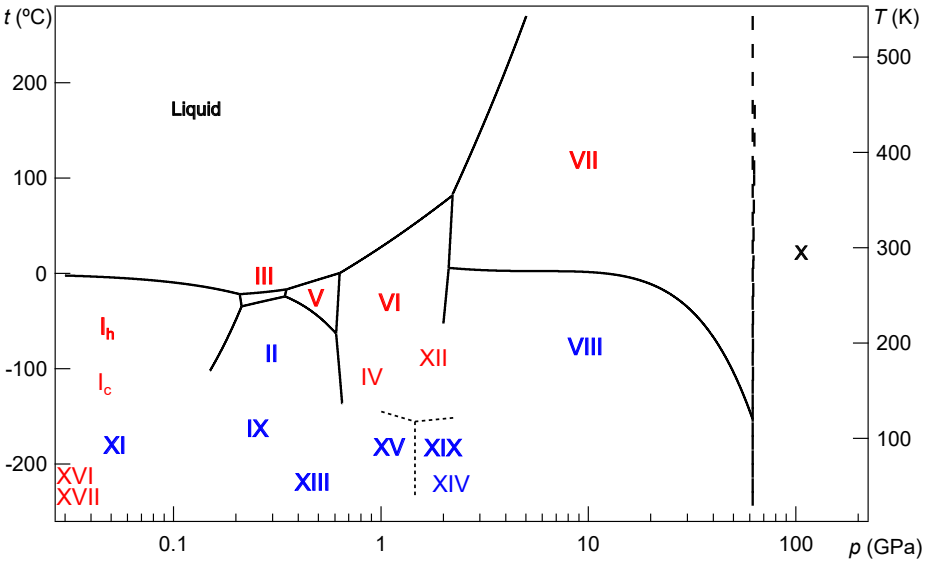

Figure 1.1: Phase diagram of ice. Thermodynamically stable phases are described in bold. Red and blue colours correspond to hydrogen disordered and ordered phases. This diagram does not distinguish partial ordering order/disorder from the complete order/disorder considering the possibility of residual hydrogen order/disorder due to the experimental limitation. Ice X, far from the hydrogen order-disorder as molecules, is written in black. Solid lines indicate phase boundary among thermodynamically stable phases. Dotted lines are the provisional boundary for hydrogen ordering of ice VI into XV or XIX. Ice XVIII is not described because its stable region locates higher pressure and temperature region.

stacking-disordered structures. They were sometimes confused are called ice I.

In addition to the network topology, the phases of crystalline ice are also classified by molecular orientations. In most crystalline phases near the ambient temperature, water molecules randomly orient in the hydrogen-bonding network (Figure 1.2). These phases are called hydrogen-disordered ice. In diffraction experiments, hydrogens are observed as distributed to the crystallographic equivalent sites with occupancies less than one (*e.g.* ordinary ice I_h[22]). The molecular configurations have similar formation energies and easily swap each other. Thus, ice favours the phases with random molecular orientations at higher temperatures for the energy gain of configurational entropy ($G = H - TS$). On the other hand, this entropy contribution diminishes at low temperatures and water molecules hence favour to align in a configuration with the lower enthalpy. These phases are called hydrogen-ordered ice but cannot obediently form by cooling except for ice II and VIII. Since molecular dynamics is suppressed at low temperatures, the molecular orientations freeze in the disordered structures without reorientation to the ordered structures. In many cases, acid or base are added to promote hydrogen-ordering into the hydrogen-ordered ices XI [23], XIII [24], XIV [24], XV [25, 26], XIX [27, 28]. The additives are considered to introduce defects

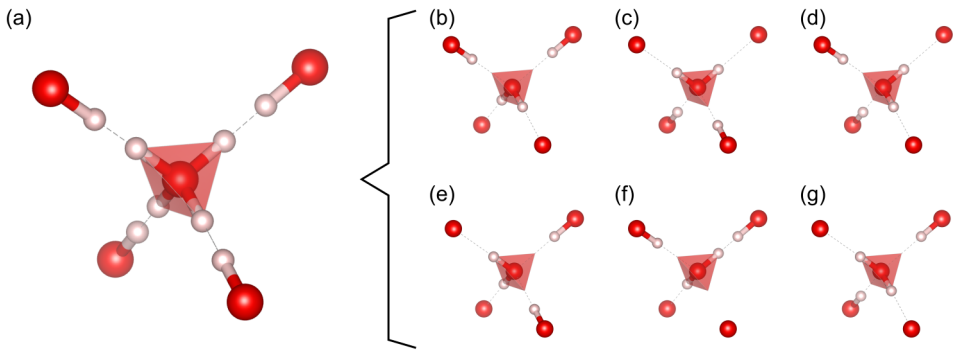

Figure 1.2: Schematic drawings of configurations of hydrogen bonds from a water molecule in tetrahedral coordination (a) in average and (b–g) snapshots. Large red and small pink balls respectively represent oxygen and hydrogen.

into the ice structure and enhance the hydrogen ordering. However, the preference between acid or base differs among ice phases, and their actual contributions are still controversial. Even using such dopant, some phases are not fully-ordered and can be regarded as partially-ordered ice as the mixture of ordered domains in different configurations, *e.g.* ice XV [29]. Because local configurations have similar enthalpy, one hydrogen-disordered phase can have multiple hydrogen-ordered counterparts like the case of ice VI with ice XV [25, 26] and XIX [28, 30]. Crystalline phases of ice have definite structures determinable by diffraction experiments, but they still have structural complexity in the topology of the hydrogen-bonding network and molecular orientations.

1.2 BCC ices

Over 2 GPa, ice seems to lose its structural variety compared to the pressure region below 2 GPa in which sixteen polymorphs exist out of the twenty. At pressures over 2 GPa, oxygen forms BCC sub-lattice and these phases (VII, VIII, X) are called BCC ice, except for ice XVIII, superionic (SI) FCC ice at extreme pT-region above thousands K and a hundred GPa [31–33]. Their BCC-based structures appear simple, but have complexity in structure and dynamic features related to hydrogen.

The hydrogen-bonding topologies of ice VII, VIII and X are explained as interpenetrating diamond-like or ice I_c networks (Figure 1.3). The crystal structures of ices VII and VIII consist of hydrogen-bonding molecular water. In ice VII, water molecules randomly orient along the orthogonal principal axes, *i.e.* a, b, and c-axes or $\langle 100 \rangle$ axes. Then, the three axes of ice VII are symmetrically equivalent. On the other hand, dipoles of water molecules align antiparallel between the nesting networks in ice VIII below 273 K [34–37]. Then, ices VII and VIII respectively have paraelectric and ferroelectric properties. One of the three orthogonal axes is no more equivalent to the other two in ice VIII, in contrast to ice VII. This unique direction is the c-axis along which water molecules align, resulting in the tetragonal symmetry of ice VIII. In contrast to ices VII and VIII as the molecular crystals, H_2O is no longer molecular water in ice X in which hydrogen locates at the exact intermediate position between the oxygens so-called hydrogen bond symmetrisation [38–43]. Then molecular vibration observed in ices VII and VIII disappeared in ice X replaced by the lattice vibration [43].

The behaviours of hydrogen in BCC ices are more complicated than the classification of the three ices VII, VIII, and X with complete hydrogen-order/disorder and bond symmetrisation. Another BCC ice is ice VII', which crystallises from amorphous ice by compression at low temperatures below 100 K [44, 45], stable regions of ice VIII. Ice VII' did not show tetragonal distortion like ice VIII but had slight features of hydrogen ordering. Ice VII' is not clear whether it is a simple mixture of ice VII and VIII or an intermediate between them as partially hydrogen-ordered ice VII. In addition, computational simulations predicted a plastic phase in which water molecules freely rotate at high temperatures [46–50]. However, these plastic phases have not been identified experimentally. Computational studies also predicted a superionic phase so-called ice VII" in which hydrogen freely move among the oxygen sublattice at higher temperatures [33, 51–53]. BCC ices in the intermediate pressure region between ice VII with molecular H_2O and ice X with hydrogen bond symmetrisation is also a target for the change of potential curve from the bimodal to the unimodal structure.

Thus, BCC ices have undetermined features relating to the behaviours of hydrogens in extreme pT-conditions. Compared to them, ice VII and VIII would be simple, as they consist of molecular H_2O. However, Ice VII

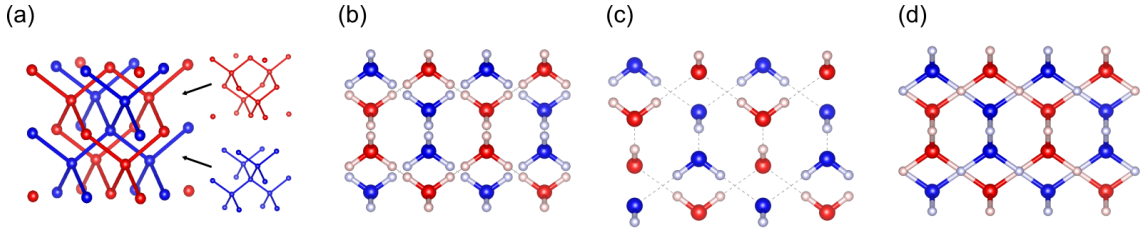

Figure 1.3: Schematic drawings of crystal structures of BCC ices. (a) Interpenetrated ice I_c networks of identical network topology with ices VII, VIII, and X. Hydrogens are omitted for clarity. Structure models of (b) ice VII, (c) ice VIII, and ice X. Topologically distinct networks are distinguished by red and blue colours.

shows various anomalous behaviours related to pressure-dependent proton dynamics: *e.g.* a sharpening of the Raman peak of its symmetric stretching mode at 11–13 GPa [54]. These phenomena are caused by a cross-over of dominant processes from molecular rotation to proton translation [55, 56]. Moreover, the entropy difference between ice VII and VIII estimated from dielectric measurements suggested partial ordering in ice VII or partial disorder in ice VIII [34, 35]. These crystalline phases have attracted much scientific interest, and it hence appears crucial to understand its detailed structure.

Many researchers have investigated the structural properties of BCC ices to understand their physicochemical features. The structure of ice VII was first derived experimentally from powder x-ray diffraction under high pressure using a piston cylinder [57], revealing the cubic structure with an oxygen BCC sub-lattice. In the x-ray diffraction studies, hydrogen positions were not determined yet, but hydrogen is deduced to be located at the intermediate between neighbouring oxygens in tetrahedral directions around each oxygen considering the plausible bonding O-O-O angles and ice rules [15]. Hydrogens in each water molecule were randomly placed to occupy two of the four sites toward the neighbouring oxygens in ice VII. Dielectric measurements found the transformation of ice VII into ice VIII by ordering the hydrogen positions (or molecular orientations) at low temperatures (below 273 K at 3 GPa [34]). In ice VIII, the orientations of water molecules are well defined: hydrogens occupy two particular sites, and molecular orientations between the interpenetrating networks are aligned antiparallel along the *c*-axis, which induces displacement of network relative to the other along the *c*-axis. The fully-ordered structure of ice VII is clear and definitely determined whereas the disordered phase, ice VII, needs some structure modelling to describe and understand the structure. These structures were examined by powder neutron diffraction [36, 37, 58], but not by single-crystal neutron diffraction.

1.3 Ionic species and water

One of the important features of water is its capability to stably comprise ionic species. As seen in nature, the sea contains plenty amount of various ions such as sodium, magnesium, chloride, sulfate, *etc.* Ion-containing water is expected to exist in icy bodies as salt-rich subsurface ocean [59, 60]. The magnetic fields of some icy bodies also suggest the existence of subsurface ocean [61–63]. The transportability and stabilisation of ions by water plays pivotal roles in biology and reaction chemistry. These salt-water coexistence fields are supposed to be a candidate for the origin of life. However, these compatible properties in liquid phase are not common in other condensed phases, crystalline ices.

The ordinary ice I is incompatible with ionic species as seen for the shelf ice. This is due to the high energetic disadvantages to form the hydrogen-bonded network with ionic species. If ionic species incorporate into ice, their strong electrostatic interactions distort the structure of the hydrogen-bonding network in ice. The distorted structure is unfavoured compared to the separation into pure ice with perfect hydrogen-bonding structure and salt, resulting in low salinity in ice I in the order of ppm except for NH_4F. Such salt expulsion are utilised for some application in freeze concentration of ice chromatography related to the interface science.

On the other hand, the BCC ices, especially ice VII, were known to incorporate ionic species [64, 65]. Ice VII was found in nature as the inclusion of diamond originated from the deep Earth [66]. The occurrence of the ion-bearing ice VII in natural conditions would affect the ion-conducting and magnetic behaviours of planets. Such salty ice VII exhibited some affected features in structure and phase behaviours induced by ionic species. Incorporation of ionic species have been simply regarded as trapping by kinetic factors. Nevertheless, an x-ray fluorescence (XRF) study suggested intrinsic compatibility of ice VII with ionic species [67]. The relation between ionic species and ice VII are still controversial and need to investigate carefully.

1.4 Neutron diffraction as a key technique for structure investigation

Neutron diffraction is a fundamental and powerful technique to examine the structure of materials. Crystal structures are the pivotal information for further investigation and discussion such as computational simulation and explanation of spectroscopic measurements. This technique allows us to observe magnetic properties and low-Z atoms, particularly hydrogen positions in materials, whereas they are not straightforwardly observable by x-ray diffraction. The positional information of hydrogen is also a key in this study. Thus, this study focus on the neutron diffraction experiments. However, light hydrogen (^{1}H) has a large incoherent scattering cross section (80.27 barn [68]) causing high background noise on diffraction patterns. Then, deuterated samples conventionally used as a substitute to avoid the incoherent scattering. In addition, deuterium (^{2}H or D) has a large scattering length (b_{coh}(D) = 6.671 fm [68]) which is beneficial for diffraction measurements under high pressure. Moreover, the scattering length does not decay according to $\sin\theta/\lambda \propto 1/d$ in contrast to x-ray diffraction (Figure 1.4). Low-d diffractions tends to have smaller crystal structure factors due to the thermal motions. In high-pressure experiments, high-pressure vessels attenuate the beams, and weak diffractions are difficult to observe. Therefore, numerous reflections are observable even for low d-spacing, which allows a structure analysis with high resolution in real space.

Neutron penetrates materials to a greater depth than x-ray. Its high penetration ability enables the observation of signals from a sample sealed in a pressure vessel. However, neutron also little interacts with the sample. Then, a larger sample volume is required than x-ray diffraction experiments, mm-size conventionally. For this reason, the generation of high pressure needs to apply large force on the sample. Thus, achievable pressure is limited below 100 GPa [69, 70] in neutron diffraction experiments compared to x-ray studies over several hundreds GPa [71–76]

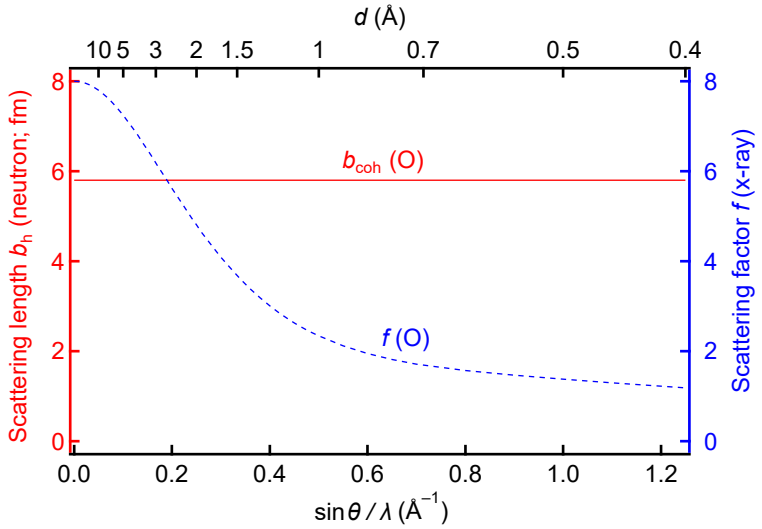

Figure 1.4: Comparison of scattering ability of oxygen. Red solid line and blue dot line respectively correspond to coherent scattering length b_{coh}(O) for neutron [68, 77] and scattering factor f(O) for x-ray [77, 78].

1.5 Objective and contents of this thesis

As a whole, water ice still has many questions related to its structural variety and complexity. Their physical and chemical properties depend on the circumstances and are difficult to examine without ambiguity. Ice VII, one of the BCC ices, seems to have a relatively simple structure but contains structural complexity and non-straightforward behaviours. This thesis aims to clarify the ambiguous properties of ice VII by providing direct and definitive information. I selected neutron diffraction techniques to investigate them from *in-situ* observation. Neutron diffraction patterns provide direct information related to structure: phase identification, volume change, lattice distortion, hydrogen ordering, and pressure estimation by the equation of state. The diffraction signals are sharper than those observed in spectroscopic approaches and are beneficial for the analyses in this thesis.

Chapter 2 describes developments of newly-designed diamond anvil cells (DACs) for single-crystal neutron diffraction. Neutron diffraction techniques were well-developed for powder samples but still limited for single-crystalline samples. I introduced promising materials to develop a new type of DACs: nano-polycrystalline diamond (NPD) anvils and Zr-based bulk metallic glass (Zr-BMG) load frames. High neutron transparency of the materials and a novel DAC design enable the observation of diffraction spots from the sample without angular limitations. The wide coverage of the DAC supports the verification of the observed diffraction intensities by the comparison of crystallographic equivalents. The simplified design of the irradiated components also allows the accurate intensity correction. A breakthrough in the experimental techniques with novel devices provides new approaching pathways to the intrinsic and fundamental properties of materials.

Chapter 3 explains investigations of the intrinsic structure of ice VII. The disordering nature of ice VII is composed of the combination of molecular orientation, hydrogen-bond formation, displacement from the average position, and some distortions affected by stimulation such as pressure, temperature, and ionic species. Moreover, these disorders have both static and dynamic features. Thus, it needs to first clarify the nascent properties of ice VII for further specific arguments for anomalous dynamic behaviours, hydrogen-bond symmetrisation, and salt incorporation. In this chapter, I conducted single-crystal neutron diffraction experiments using the newly-developed DAC in Chapter 2 and powder neutron diffraction using the MITO system [79]. These high-pressure devices dedicated for *in-situ* diffraction experiments provides high-quality information in reciprocal space sufficient for detailed structure analysis. Two types of structure analyses were applied for the diffraction data to obtain the information on the disordered structure of ice VII beyond the limitation in the conventional structure refinements using structure models.

Chapter 4 treats the relationship of incorporation of ionic species into ice VII and the physical properties of ice VII affected by the incorporation. Previous studies on salty ice VIIs varied in species of ions and their concentration. Moreover, the observed properties of salty ice VII were distinct. For example, even the volume expansion/shrink differed among the papers and was too complicated for systematic understanding. The largest gap among the reported salty ice VIIs is the experimental path: one crystallised via amorphous at low temperature with high concentration of ionic species and one crystallised from solution at ambient temperatures with lower concentration. Considering that salty ice VII is in a kinetically-trapped and unstable state in non-equilibrium conditions, ice would expel ionic species and salts or salt hydrates forms by relaxation by heating or decompression. Then, in this chapter, I examined the transient behaviours from the salty ice VII with high concentration to salty ice VII with less concentration by continuous *in-situ* diffraction experiments. The successive experiments provide an aspect to overview the complicated behaviours of ice VII. The neutron scattering techniques are beneficial to observe the hydrogen ordering features affected by the distortion induced by the strong electrostatic interaction by the incorporated ionic species in addition to volume changes.

Each chapter contains its essential theory and procedures in addition to instrumental and scientific topics. Appendix provides more fundamental, practical and detailed information related to the diffraction experiments and coexisting hydrates.

2 Development of diamond anvil cells for single-crystal neutron diffraction

This chapter is not available for publication as it will be published in a journal within the next five years.

3 Disordered structure of pure ice VII

This chapter is not available for publication as it will be published in a journal within the next five years.

4 Two types of salty ice VII

This chapter is not available for publication as it will be published in a journal within the next five years.

5 Concluding remarks

In my thesis, I described technical developments of DACs for single-crystal neutron diffraction and scientific topics about pure and salty ice VII. This thesis is based on the fundamental scope to investigate the simple molecules in bulk phase by neutron diffraction experiments under high pressure. The technical developments in *in-situ* measurement apparatuses enabled to clarify the observation of the complicated materials in detail.

Newly developed DACs were described in Chapter 2. The DACs were designed for single-crystal neutron diffraction under high pressure. Their design concept is to open the observable directions among almost all the solid angles. Key points are components around the sample space: NPD anvils and Zr-BMG cylinders. Both materials have high neutron transparency and allow the incident and diffracted beams to pass through them with sufficient intensities for measurement. Moreover, both do not cause serious parasitic diffractions, problematic in many *in-situ* diffraction studies. Thus, numbers of diffraction spots are observable and easily identified. The wide coverage of reciprocal space also has the advantage to evaluate the observed diffraction intensities by comparing crystallographic equivalents. The component geometry is expected to generate a pressure of 8 GPa and its durability was examined in offline tests with maximum pressure up to 4.5 GPa.

Test experiments on single-crystalline NaCl at the D9 diffractometer of the ILL and NH_4Cl at the BL18 of the MLF J-PARC demonstrated low background levels and absence of Bragg spots other than the specimen. In both experiments, the diffraction patterns for the samples stored in the DAC showed comparable refinement results with those out of the DAC. High-pressure diffraction experiments on ice VI at BL18 also resulted in structure refinements with sufficient quality.

Optical accessibility enables *in-situ* single-crystal growth from solution as demonstrated in the case of ice VI. Such approaches are necessary for molecular crystals with structural variety under high pressure. Moreover, molecules also form solvates with various compositions. Structural analyses of these flexible and complicated crystals need enormous diffraction intensities. While the cell still needs to be improved for studies at higher pressures, the developed DAC is expected to be advantageous for structure refinements from the *in-situ* high-pressure experiment.

Detailed structure analyses on pure ice VII were described in Chapter 3. To reduce the biases by specimen type, single-crystal and powder neutron diffraction experiments were conducted at 2.2 GPa and 298 K using the developed DAC and MITO system [79] for the MEM analysis. The MEM analysis showed clear distributions of atoms aside from the average potions in ice VII. Those from single-crystal and powder data showed similar features of the ring-like distribution of deuterium and oxygen displacements along $\langle 111 \rangle$. Observed distributions were consistent with the previously proposed displacement models [58, 133], while the ring-like and potentially elongated feature of deuterium was first observed experimentally, highlighting the insufficiency of explanation with simple point-like structure models.

Correlation functions were derived from the total scattering profiles of powder diffraction. This analysis revealed that the water molecules in ice VII are identical to those in ice VIII in contrast to conventional Rietveld refinements. This would be similar to the case for ice I in which elongated O-D distances derived in conventional diffraction studies were replaced by slightly shorter distances from PDF analysis [11]. Moreover, the local structure of ice VII was completely different over the size of the unit-cell of ice VII. This implies that water molecules in ice VII are almost fully random-oriented and have little ordered structure even in short-range.

In a pressure region at *ca.* 11 GPa, dominant hydrogen dynamics are expected to change from the molecular rotation to the intermolecular translation of hydrogens [30, 55, 56]. The structural features of ice VII revealed in this study have the potential to clarify such behaviours. Further experiments at higher pressures would provide more information on the relation between the atomic distribution and the dynamic behaviours of ice VII. In practice, the single-site model can satisfactorily reproduce the diffraction patterns of ice VII as mentioned in the introduction. However, the detailed disordered structure of ice VII is related to intrinsic distortion from the completely symmetric structure. It would be related to tolerance against distortion externally induced such as by salt incorporation. Thus, the intrinsic structure of ice VII is necessary to deal with its compatible feature with ionic species.

The behaviours of salty ice VII was described in Chapter 4. The $MgCl_2$:D_2O = 1:25 (mol) solutions successfully vitrified by cooling to 100 K from room temperature and 0.6–0.7 GPa. Successive compression at 100 K resulted in saline amorphous with broad diffraction peak at lower-d than one before compression. According to heating at high pressures, the amorphous peak became sharper like the case of annealing of pure amorphous ice VHDA [169].

These saline amorphous remained in wider pT-regions than pure ice [45] until crystallisation at 260 K and 4 GPa in path A and 200 K and 6.7 GPa in path B. Surprisingly, further annealing at higher temperatures resulted in the splitting of ice VII peaks into two with different excess volumes. α-VII, which crystallised from saline amorphous, retained its excess volume larger than 5% while β-VII, which emerged after annealing, had smaller excess volumes. Their behaviours were also different in hydrogen ordering, such as scarcely ordered α-VII in contrast to the gradual increase of ordered feature of β-VII according to annealing. α-VII finally disappeared, and the excess volume of the remaining β-VII gradually decreased to 0%. According to the volume decrease of β-VII, diffraction peaks from salt hydrates became observable, indicating salt expulsion from salty ice VII during the relaxation of β-VII.

Many things remain ambiguous on salty ice VII, but distinct behaviours were clarified for those classified as α- and β-VII in this study. Further systematic analyses on the correlation of $MgCl_2$ concentration of salty ice VII will provide further information about the difference of α- and β-VII.

Ice VII is regarded as a simple phase compared to other ice phases with complicated network topology. This study clarifies their intrinsic complexity in both pure and salty. The salt compatibility with ice VII is actually related to kinetic trapping under high pressure and low temperature. On the other hand, the distinct two types of salty ice VII imply the structural variety of ice VII. These are considered to be the structural variation in distortion by salt incorporation. In other words, the incorporation scheme would be different slightly.

In this thesis, the structure and behaviours of pure and salty ice VII were investigated independently. Nevertheless, the intrinsic structure of ice VII are inevitably related to its dynamic behaviours and the stability or tolerance to the distortion induced by the external stimulation, such as the incorporation of ionic species. The volume change discussed in Chapter 4 was mainly based on the averaged and periodic structure, such as the single-site model. The derived distortion is also the result of spatial and time average. It does not directly represent the local structure around the incorporated ionic species. The tolerance of ice VII to hold the ionic species in a few percent would come from the structural tolerance as the whole network. The distortion induced by the electrostatic interaction by ionic species can be cancelled by the neighbouring distortion by other ionic species of water molecules. Related to the local structure around the ionic species, they attract the neighbouring water molecules more strongly than the other water molecules by the electrostatic interaction. These interactions appear to induce locally ordered embryos in different ways from ice VIII as suggested in the case of salty-ice VII ($NH(D)_4F$) [179]. Thus, the incorporation of ionic species has a probability to modify the relative stability of different configurations as the hydrogen-ordered counterpart of ice VII. The actual application needs some further improvements on measurement and analysis techniques, but the detailed analyses described in Chapter 3 would provide more direct information of the disorder or order of the local structures in ice VII induced by the ionic species.

From a different aspect, salt hydrates can be a good comparison to discuss the structure of water molecules around ionic species. The main reason of the difficulty to clarify the local structure around the ionic species in salty ice VII is because the incorporation occurs randomly. On the other hand, salt hydrates have periodic structures, which can be elucidated from the conventional structure analyses from diffraction experiments. Especially, most water-rich hydrates, containing more than six water molecules per cation which is fully hydrated, forms hydrogen-bonding networks consisting of coordinating/interstitial water molecules and anions. Under high pressure, salt hydrates have unique bonding structures or hydration numbers uncommon at ambient pressure [125–127, 131]. Their structure analyses can experimentally provide the information of interatomic distances and angles under high pressure, and support the discussion from computational approaches. However, these high-pressure phases of multicomponent crystals are unstable at ambient pressure and tend to have complicated structural features. Therefore, single-crystal neutron diffraction is a prospected technique to investigate the bonding structure including the hydrogen (deuterium) atoms. The developed DAC described in Chapter 2 provides the practical approach to investigate them from *in-situ* measurements.

A Fundamental theory of diffraction

A.1 Reciprocal space for crystalline materials

Diffraction can be regarded as a kind of projection of structures in real space into structure factors in reciprocal space. Their relation can be explained as the Fourier transformation mathematically. Crystal is defined as an entity in which components align periodically in a long-range order. The definition of the term "crystal" has changed in 20–21st centuries. Now, the term contains a wider range of solids based on the central idea of order in either real space or reciprocal space. Here, pseudo-crystals and modulated structures are out of the interest of this study. The crystal structure can be reformed by the combination of three-dimensional periodicity of structural units (unit cell) and aperiodic terms in each unit cell. Then, the Fourier transformation can be written in the following formula for crystal structure factor $F(\boldsymbol{k})$ (Equation (A.1)) by extracting the Laue function which comes from the periodicity of the unit cell.

$$F(\boldsymbol{k}) = \int_{\text{unit cell}} f(\boldsymbol{r})\rho(\boldsymbol{r}) \exp(-2\pi i \boldsymbol{k} \cdot \boldsymbol{r}) d\boldsymbol{r} \tag{A.1}$$

$\rho(\boldsymbol{r})$ corresponds to density of scattering factors depending on the radiation type and $\boldsymbol{k}$ is a scattering vector defined as $\boldsymbol{k} = \boldsymbol{k}_1 - \boldsymbol{k}_0$ from the wave vectors of incident ($\boldsymbol{k}_0$) and scattered ($\boldsymbol{k}_1$) beams which have the norms of the inverse of their wavelengths. The scattering vector, $\boldsymbol{k}$, has information of direction and wavelength of the beams. This study only treat the elastic scattering in which the wavelengths of the beam does not change before and after the scattering, *i.e.* $|\boldsymbol{k}_0| = |\boldsymbol{k}_1|$. The scattering factor is called the scattering length for neutron diffraction because of it has inverse unit of length. The diffraction intensity for each reciprocal lattice point corresponds to the squares of the norms of its crystal structure factor. In diffraction-based structure analysis, the structure in real space is discussed based on the observed diffraction intensities with statistical approach to reduce the errors between measurement and calculation from the model. In conventional structure refinements, $\rho(\boldsymbol{r})$, continuous function of $\boldsymbol{r}$ is replaced by a single value, b_i, dependent on the species of atom, i, and atomic positions, $\boldsymbol{r}_j$, as in Equation (A.2). In other words, the distribution is simplified as discrete sites assigned to specific atoms.

$$F(\boldsymbol{k}) = \sum_i \sum_j^{\text{unit cell}} b_i \exp(-2\pi i \boldsymbol{k} \cdot \boldsymbol{r}) \tag{A.2}$$

A.2 Ewald sphere to describe diffraction conditions

Diffraction intensity comes from the superposition of the beams scattered from the scatterer. Thus, diffraction has a strong intensity in specific conditions in which scatterings in different paths coherently contribute to the diffraction when Equation (A.3) is fulfilled. In this condition, the Laue functions become non-negligible and have a significantly large value. The diffraction can be observed as a Bragg spots. This explanation can be redefined as in (A.4) using reciprocal lattice vectors ($\boldsymbol{a}^*, \boldsymbol{b}^*, \boldsymbol{c}^*$) known as the Laue condition.

$$\boldsymbol{k} \cdot \boldsymbol{x} \in \mathbb{Z} \ (\boldsymbol{x} = \boldsymbol{a}, \boldsymbol{b}, \boldsymbol{c}) \tag{A.3}$$

$$u, v, w \in \mathbb{Z} \ (\boldsymbol{k} = u\boldsymbol{a}^* + v\boldsymbol{b}^* + w\boldsymbol{c}^*) \tag{A.4}$$

Thus, reciprocal lattice points ($\boldsymbol{d}^* = h\boldsymbol{a}^* + k\boldsymbol{b}^* + l\boldsymbol{c}^*$) defined with integer indices ($h, k, l \in \mathbb{Z}$) automatically fulfil the Laue condition. The Laue condition can be visualised by the Ewald sphere in 3-dimensional diffraction reciprocal space. Figure A.1 shows 2D-projected Ewald sphere in which scattering vector $\boldsymbol{k} = \boldsymbol{k}_1 - \boldsymbol{k}_0$ coincides with one reciprocal lattice vector $\boldsymbol{d}^*_{210} = 2\boldsymbol{a}^* + \boldsymbol{b}^*$. In this case, the scattering vector satisfies the Laue condition. The conditions vary by the wavelength, λ, *i.e.* the radius of the Ewald sphere, $1/\lambda$, and the relative orientations of beams. Then, the Laue conditions can be explained as the following two requirements.

(a) The reciprocal lattice is on the Ewald sphere.

(b) The wave vectors of the incident and diffracted beam are in the observable directions.

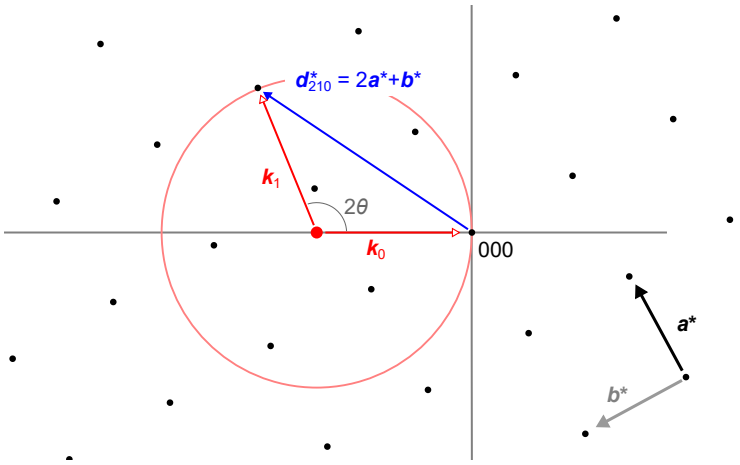

Figure A.1: Ewald sphere for reciprocal lattice with cubic symmetry projected on $\boldsymbol{a}^*\boldsymbol{b}^*$ plane. Red circle corresponds to the projected Ewald sphere while black dots does to the reciprocal lattice points of the crystal.

A.2.1 Observable reciprocal space in principal

In conventional single-crystal diffraction, the crystalline specimen can be arbitrarily rotated into the desired orientations neglecting a small solid angle around the mounting pin. In this case, requirement (b) is negligible and only requirement (a) needs to be taken into account. Then, the observable reciprocal space is those with $|\boldsymbol{d}^*| = 1/d < 2/\lambda$ as shown in Figure A.2. Thus shorter-wavelength is preferred for structure analysis with the high spatial resolution by observation in wider reciprocal space in principal. In actual measurements, the observable reciprocal space is limited by the signal-to-noise ratio. In low-d region, the diffraction intensity drastically decay by Lorentz factor (described in Appendix B). The intensity decay in the low-d region is more serious for x-ray study because of the decay of scattering factor as described in Chapter 1. On the other hand, the high-d (*i.e.* low-d^*) diffractions from crystals with large unit cells are difficult to measure with beams with short-wavelength because their diffraction angles 2θ is small and diffuse scattering from the direct beam would overwhelm the diffraction.

Single-crystalline specimens rarely satisfy the diffraction condition for the requirement (b). On the other hand, powder specimens can be interpreted as simultaneous measurements of tiny single crystals in different orientations. The reciprocal lattice points form spheres centred at the origin, the 000 reciprocal lattice point. Then, the spheres

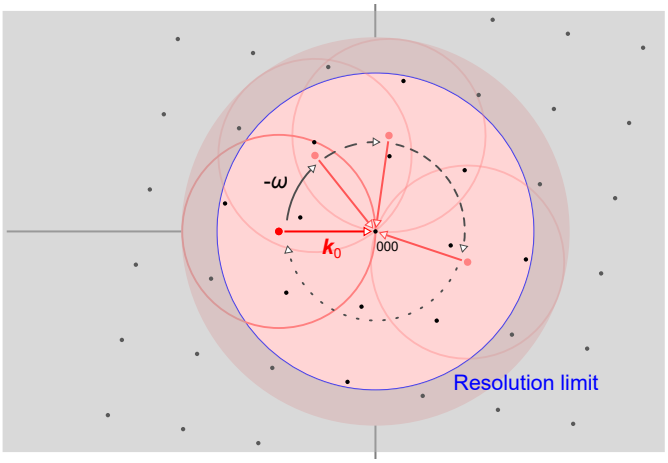

Figure A.2: Observable reciprocal space described using Ewald sphere. The observable region is the cross-section of the surface of the Ewald sphere during its free rotation with a fix at 000 point. In this cross-section, the observable region is shaded by red. The arrows correspond to the rotation of the Ewald sphere by $-\omega$ around the axis normal to the plane on 000. This clockwise rotation corresponds to anti-clockwise rotation of reciprocal space *i.e.* sample crystal by ω in real space. The area shaded by grey indicates unobservable regions because of the resolution limit described by the blue circle.

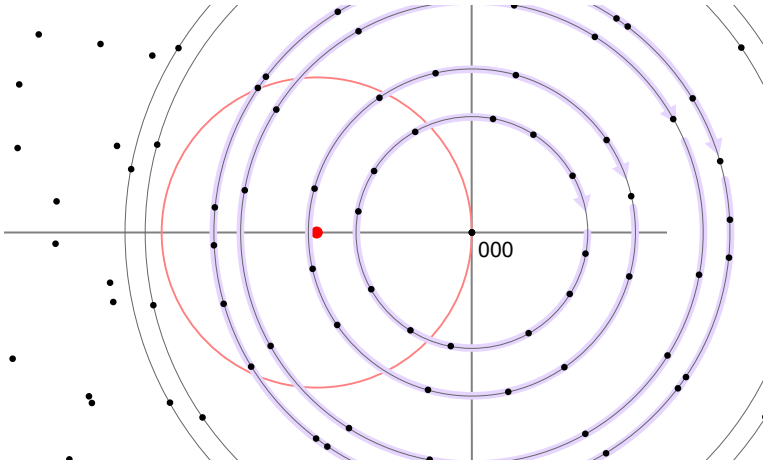

Figure A.3: Ewald sphere for reciprocal lattice for powder specimen. The red circle corresponds to the projected Ewald sphere while black dots represent the reciprocal lattice points of tiny crystals. The reciprocal lattice points were distributed on a surface of each sphere centred at the origin, the 000 reciprocal lattice point, with a radius of d^*.

with lower-d^* than the observable limit from wavelength cross with the Ewald sphere. Then the ring-like diffraction can be observed in 2-dimensional detectors, known as the Debye rings, instead of point-like Bragg spots. However, reciprocal lattice points with the same d^*, such as crystallographic equivalents, degenerate into a single sphere. The spheres lose the orientational information and only retain the one-dimensional information, d-spacing. Then the reciprocal lattice points overlap eventually when their d-value is not separated well compared to the experimental resolution. This is the serious disadvantage of powder diffraction in contrast to the observation of discrete Bragg spots in single-crystal diffraction.

A.2.2 Accessible reciprocal space in diffraction experiments

To observe the diffractions, diffractometers are designed to make the reciprocal space fulfil the requirements (a) and (b) in different ways.

(1) Angle-dispersive diffractometer with continuous wave (CW) neutron

In angle-dispersive diffractometers, while diffraction patterns are collected in different directions with fixed wavelength λ of the neutron. It corresponds to finding reciprocal lattice points along the Ewald sphere of a fixed radius of $2/\lambda$ varying the orientation of $\boldsymbol{k}_1$ with respect to the reciprocal lattice. In single-crystal diffraction measurement, specimens are rotated to fulfil the requirements to obtain each pattern in individual orientation (Figure A.4a). The peak intensity can be obtained by the accumulation of each diffraction spot individually (Figure A.4b). The four-circle diffractometer with the Eulerian cradle at the D9 of the ILL is one of them. In the D9 beamline, the desired wavelength of the neutron is extracted using a monochromator from the continuous white wave produced by a reactor source. In this setup, accurate peak intensities can be extracted by rotational scan by evaluating the crossing of a reciprocal lattice point through the Ewald sphere surface.

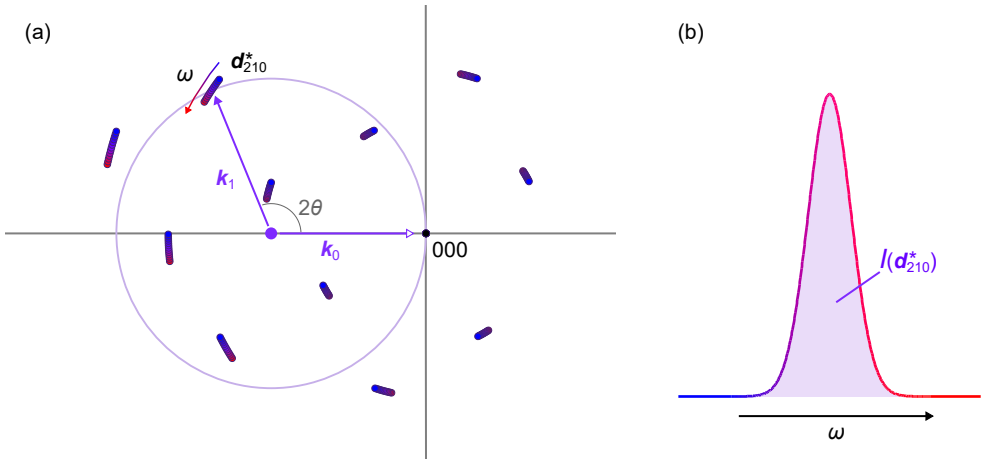

Figure A.4: (a) Observable reciprocal space in angle-dispersive diffraction with single-crystalline sample by rotating the specimen. The colour graduation from blue to red corresponds to the rotation by ω along the axis perpendicular to the plane centred at 000. (b) Representative diffraction intensity for $\boldsymbol{d}^*_{210}$ in ω-scan.

(2) Energy-dispersive diffractometer with white neutron

Another main technique is to scan the wavelength *i.e.* energy of beam. This scanning corresponds to observing fan-shaped regions spreading from 000 with certain directions as shown in Figure A.5. This approach is quite beneficial for powder samples whose reciprocal lattice forms concentric spheres. In x-ray diffraction, diffraction patterns are collected depending on energy. For neutron studies, time-of-flight type diffractometer is commonly used. In this diffractometer, the neutron wavelength is calculated as de Broglie wavelength, $\lambda = h/m_n v$, from neutron speed, v, with Planck constant, h, and neutron mass, m_n. The neutron speed can be estimated from the time-of-flight.The BL11 beamline [136] at the MLF J-PARC is one of them with a spallation source [215].

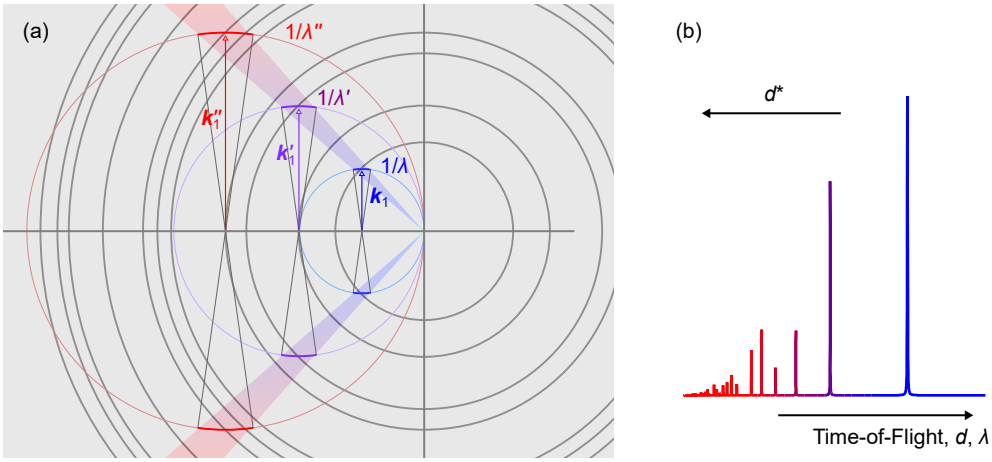

Figure A.5: (a) Observable reciprocal space in energy-dispersive diffraction with powder sample for $2\theta = 90°$. The colour graduation from blue to red corresponds to the wavelengths of beams from long to short ($\lambda > \lambda' > \lambda''$, $|\boldsymbol{k}'_1| < |\boldsymbol{k}'_1| < |\boldsymbol{k}''_1|$). Unobservable directions are shaded by grey. (b) Representative diffraction profile.

(3) Laue-TOF diffractometer

In Laue diffractometer, diffraction patterns are collected in various directions of diffracted beam $\boldsymbol{k}_1$ with white neutron. In this case, d-space cannot be determined directly from the diffraction pattern and diffractions inevitably overlap with their integer multiples like hkl and $nk\ nk\ nl$. Then, the combination with energy dispersive measurement enables the decomposition of diffraction pattern in d-space. The BL18 beamline [118] of the MLF, J-PARC one of such Laue-TOF diffractometer with the pulsed neutron source. In practice, time-resolved detectors with wide coverage of solid angles are necessary for three-dimensional observation for two in orientation and one in time-of-flight *i.e.* wavelength.

A.2.3 Observable reciprocal space in high pressure experiments

If the diffraction geometry has no angular limitation as an ideal condition (Figure A.2), the volume of observable reciprocal space is that of a sphere with a radius of $2/\lambda$ to be $V_{\mathrm{full}} = (4/3)\pi(2R)^3$ as a function of radius of the Ewald sphere ($R = 1/\lambda$). Here, monochromatic neutron beam is assumed for simplicity. For the case of diffractometers using white neutron beam like the Laue diffractometer, the observable regions are extended analogously to discussed above for the energy-dispersive diffractometer.

In actual experiments, neutron beams cannot come from or be observed in certain directions. The limitation of accessible direction hence causes difficulty to cover the reciprocal space in high-pressure experiments. This requirement can be described as orientational constraints for $\boldsymbol{k}_0$ and $\boldsymbol{k}_1$ against the reciprocal lattice. Thus, the observable reciprocal space can be derived as the intersection of the valid surface of the Ewald sphere when the sphere rotates around the origin, 000 reciprocal lattice point, under the directional constraints. Figure A.6 shows the representative geometries of DACs in single-crystal neutron diffraction and their observable reciprocal space. The observable diffractions limited by the DAC geometry can be estimated by geometrical calculation in the reciprocal space using the Ewald sphere. First, DACs in the transmission geometry can be an example as a simple case. Let z-axis along the compression axis, and its observable reciprocal space is cylindrically symmetric around the z-axis. Then, the observable volume, V_1^*, can be calculated as an intersection of the shaded area in Figure A.6c rotated along the z-axis. For the one with the half opening angle of $\Theta = 40°$ each from the central compression

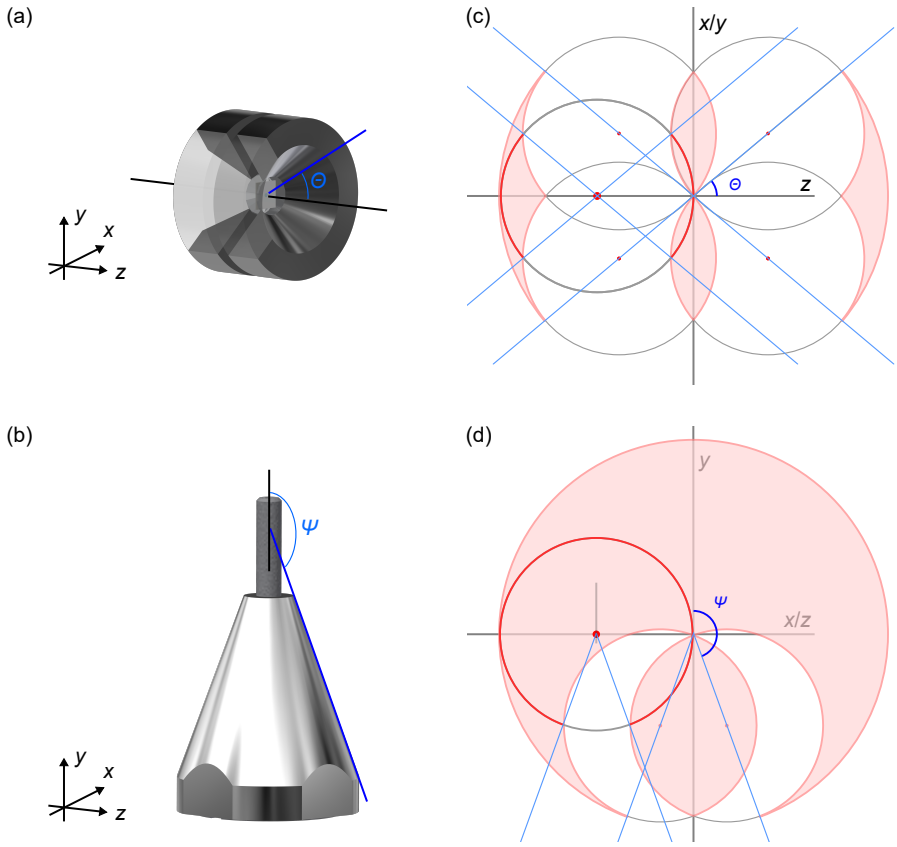

Figure A.6: Schematic image of angular limitations of (a) DACs in transmission geometry and (b) the developed DAC in Chapter 2. The diffraction geometries are defined to orient y-axis along the vertical line, z-axis on the horizontal plane in which the incident neutron beam $\boldsymbol{k}_0$ comes in the principal orientation, and x-axis to be in the right-handed system. (c) The cross-sections of the observable reciprocal spaces, for (a) with opening half angle $\Theta = 40°$ and (d) for (b) with the opening cone angle $\Psi = 160°$ with a monochromatic wavelength of neutron beam. Red arcs indicate the part of the Ewald circle in observable directions when the incident neutron beam $\boldsymbol{k}_0$ come along the z-axis. The shaded areas in red correspond to the observable region derived as the intersection of the observable arcs when the Ewald sphere rotates around the axis perpendicular to the projected plane at the origin, 000 of the reciprocal lattice, under the directional constraints on $\boldsymbol{k}_0$ and the diffracted beam, $\boldsymbol{k}_1$. The resolution limit is not taken into account for clarity.

axis, common geometry as Boehler almax anvils [93], diffraction experiments can cover only 8% of the full sphere from Equation (A.5) including the back scattering geometry. The second derivative of Equation (A.5) with respect to Θ is $9\sin^2\Theta\cos\Theta$, so that the observable region does not increase significantly below the inflection point at $\Theta = 45°$. With a larger half opening angle of $\Theta = 60°$, 31% of the full sphere becomes observable.

$$\begin{aligned} V_1^* &= 2\int_{2R\cos\Theta}^{2R} \pi[(2R)^2 - x^2]dx \\ \frac{V_1^*}{V_{\text{full}}} &= \frac{2 - \cos\Theta(3 - \cos^2\Theta)}{2} \end{aligned} \tag{A.5}$$

In a similar way, the observable reciprocal space can be estimated for the new type of DAC developed in Chapter 2. The developed DAC has little angular limitation in diffraction geometry except for conical region spreading from the sample position. Thus, the neutron beam can come from and go to the directions in the angle from the vertical y-axis along the compressing direction below the opening half angle, Ψ. The observable region in reciprocal space for the developed DAC also has the cylindrical symmetry around the y-axis. The three-dimensional observable region is an intersection of the shaded area in Figure A.6d rotated along the y-axis with the cone angle of 40°. The integrated volume, V_2^*, with respect to the full sphere can be formulated as Equation (A.6). The developed DAC with the opening half angle $\Psi = 160°$ can cover 80% of the full sphere.

$$\begin{aligned} V_2^* &= \int_{2R\cos\Psi}^{2R} \pi[(2R)^2 - x^2]dx + \int_{R\cos\Psi}^{-R\cos\Psi} \pi\left(\sqrt{R^2 - x^2} - R\sin\Psi\right)^2 dx \\ &\quad - \left[\int_{R\cos\Psi}^{R} \pi\left(\sqrt{R^2 - x^2} + R\sin\Psi\right)^2 dx - \int_{-R\cos\Psi}^{R} \pi\left(R\sin\Psi - \sqrt{R^2 - x^2}\right)^2 dx\right] \\ &= \int_{2R\cos\Psi}^{2R} \pi[(2R)^2 - x^2]dx - 2\int_{R\cos\Psi}^{R} 2\pi R\sin\Psi\sqrt{R^2 - x^2}dx \\ \frac{V_2^*}{V_{\text{full}}} &= \frac{2 - \cos\Psi(3 - \cos^2\Psi)}{4} - \frac{3}{16}\sin\Psi\left[\Psi - \frac{1}{2}\sin(2\Psi)\right] \end{aligned} \tag{A.6}$$

In addition, some diffraction spots are crystallographically equivalent to others from the crystal symmetry. For example, 100 diffraction of ice VII (space group $Pn\bar{3}m$) has 5 equivalent diffractions (*i.e.* $100, \bar{1}00, 010, 0\bar{1}0, 001, 00\bar{1}$). These equivalences depends on the symmetry of the crystalline sample. On the other hand, the Friedel pairs, hkl and $\bar{h}\bar{k}\bar{l}$, have the identical diffraction intensities because the observed diffraction patterns loses the information of phase. It needs special approach to examine the difference between the Friedel pairs, such as the anomalous scattering using a specific wavelength of beam. Identifying reciprocal lattice points with their Friedel pairs, the half of the reciprocal space is at least enough for structure analysis, even though the observed diffraction intensities are preferred to be examined by comparing these equivalent diffraction intensities. In that case, the developed DAC can cover the whole necessary and principally accessible reciprocal space. In practice, the observable diffraction spots are also limited by the resolution limit. The resolution limit is determined by the signal-to-noise ratio depending on the performance of the diffractometers, the intensity of the signal from the sample related the sample volume and components, and interference by high-pressure cells such as attenuation and background scattering. It depends on the experimental conditions, but the covered area compared to the region defined from the resolution limit is slightly different.

A.2.4 Multiple scattering

In structural analysis, the elastic and coherent scatterings are taken into account. In addition, the scattering is assumed to occur once during the flight. However, diffracted beams by materials are sometimes diffracted again. This event is not accidental but theoretically possible considering the Laue conditions as shown in Figure A.7 When neutron is diffracted as $\boldsymbol{k} = \boldsymbol{d}^*_{2\bar{1}0}$, the diffracted beam $\boldsymbol{k}_1$ travel through the crystal and behaves as another incident beam $\boldsymbol{k}'_0 = \boldsymbol{k}_1$. Then, $\boldsymbol{d}_{\bar{2}\bar{1}0}$ the Friedel pair of $\boldsymbol{d}_{210}$ is definitely on another Ewald sphere defined for $\boldsymbol{k}'_0$. The neutron diffracted twice $\boldsymbol{k}'_1$ orients towards the same direction of the original incident beam $\boldsymbol{k}_0$. This multiple

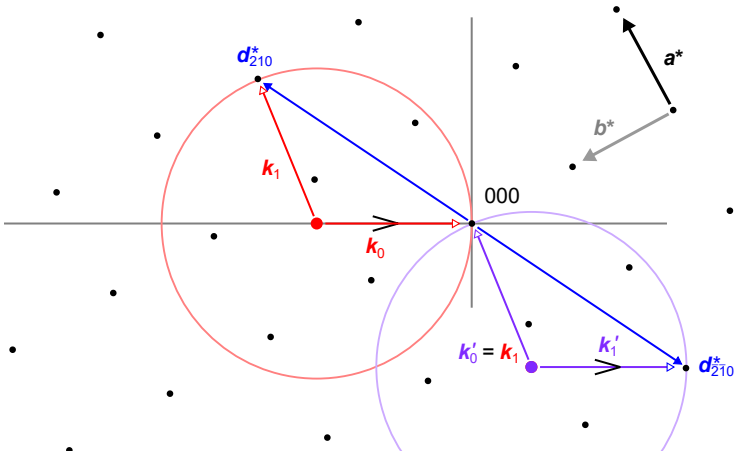

Figure A.7: Schematic image of multiple scattering with Ewald sphere. Red and violet colours correspond to the diffraction conditions for the first and second diffraction events. The diffracted beam $\boldsymbol{k}_1$ behaves as an incident beam for the second diffraction. In this case, the Friedel pair of the first diffraction automatically fulfil the Laue condition from their relation in inversion symmetry. Resolution limits are not taken into account for clarity.

scattering is negligible for tiny crystals because of the high penetration ability of neutron but becomes serious for large crystals or highly interactive beams such as electron beam.

Diffraction events more than once can also take place accidentally among different crystals *i.e.* polycrystalline samples or those by the sample container. Such additional scattering by the vessel is a kind of intensity attenuation and is briefly described in Appendix B.

A.3 Collimation of neutron beams

Since anvils and gaskets are directly attached to the sample, diffracted neutrons from the high-pressure cell inevitably contaminate the observed signals in high-pressure experiments. Moreover, the Zr-BMG cylinders are also irradiated in our cell design. BN collimator with a diameter of 0.8 mm was placed upstream of the neutron beam from the sample to reduce the background diffraction from the DAC components, especially from NPD anvils. The incident-beam collimator was aligned line using a camera. The sample was also aligned to be at the rotation centre of the ω-goniometer. The sufficiency of the alignment can be examined by data accumulation for at most several minutes because no spots can be observed other than those from the sample. Such fast evaluation can reduce the time for centring.

In contrast, diffracted beams are not collimated in this setup. Although it is technically possible to eliminate such contaminating diffractions using radial collimators [216, 217], such as used in high-pressure powder diffraction experiments at BL11 (PLANET) of the MLF J-PARC [136], the collimation of diffracted beam has a risk of the intensity decrease at the edges of the collimating region. Discrete spot peaks in single-crystal diffraction are strongly affected by the truncation of diffracted beams and are difficult to examine compared to powder lines that can be integrated among two-dimensional Debye rings. Moreover, this risk is even higher because a quite small gauge volume is required for high-pressure experiments. As a whole, it is supposed to be less effective in practice to introduce radial collimators for this case.

A.4 Conventional structure analyses

For comparison with the analytic procedures conducted in Chapter 3, the conventional structure refinement for power diffraction profiles is briefly explained here. Conventional structure analyses refine structure models. In more detail, centres of atomic positions and their distribution are prospected to be represented by a relatively simple model, such as isotropic spheres and ellipsoids. The parameters to describe the models are refined by the least-square procedures. The errors of the obtained parameters are derived from the error matrix in these regressing procedures and are usually underestimated. The reliability of refined structure models can be evaluated by several statistical measures derived from the observed diffraction patterns and the calculated diffraction intensities. Their definition is provided by IUCr union [218] for crystallographic information file (CIF) entry and by each analysis software for specific values.

A.4.1 Statistical measures for single-crystal diffraction

In single-crystal diffraction, discrete diffraction spots can be measured, and individual diffraction intensity can be directly derived from experiments. Thus, structure refinement procedures can be conducted with the tabulated intensities extracted by three-dimensional peak fittings of the diffraction patterns. Structure refinement for single-crystal data were conducted using *SHELXL* [119] and *JANA2020* [121].

The quality of observed diffraction intensities are indicated by R_{equiv} called R_{int} in *SHELXL* as the consistency in intensities of symmetry-equivalent diffractions (Equation (A.7)) and R_σ called R_{merge} in *Jana2020* from uncertainty of diffraction intensities (Equation (A.8)). The refinement results of structure models can be evaluated by R and R_w, and S. R-factor indicates the relative difference between the observed structure factors (Equation (A.9)) and is called R_1 and R_{obs} in *SHELXL* and *JANA2020*, respectively. R_w represents the weighted consistency of them and is called $wR2$ (Equation (A.10)) and wR^2_{obs} in *SHELXL* and *JANA2020*, respectively. S corresponds to a measure to evaluate the refinement procedure considering the sufficiency of observed numbers of diffraction intensities N_k and refined parameters N_{param} (Equation (A.11)) and called goodness of fit for the least square. The weight, $w(\boldsymbol{k})$, is derived from observed structure factor, $F_{\mathrm{o}}(\boldsymbol{k})$, its uncertainty, $\sigma F_{\mathrm{o}}(\boldsymbol{k})$, and calculated structure factor, $F_{\mathrm{c}}(\boldsymbol{k})$. The combination with $F_{\mathrm{c}}(\boldsymbol{k})$ reduces statistical bias [219]. The intensity, I, is replaced by squared structure factors used for regressing procedures in *SHELXL*.

$$R_{\mathrm{equiv}} = \frac{\sum_{\boldsymbol{k}} |I_{\mathrm{o}}(\boldsymbol{k}) - I_{\mathrm{ave}}(\boldsymbol{k}_{\mathrm{equiv}})|}{\sum_{\boldsymbol{k}} |I_{\mathrm{ave}}(\boldsymbol{k}_{\mathrm{equiv}})|} \tag{A.7}$$

$$R_\sigma = \frac{\sum_{\boldsymbol{k}} \sigma I_{\mathrm{o}}(\boldsymbol{k})}{\sum_{\boldsymbol{k}} |I_{\mathrm{o}}(\boldsymbol{k})|} \tag{A.8}$$

$$R = \frac{\sum_{\boldsymbol{k}} |F_{\mathrm{o}}(\boldsymbol{k}) - F_{\mathrm{c}}(\boldsymbol{k})|}{\sum_{\boldsymbol{k}} |F_{\mathrm{o}}(\boldsymbol{k})|} \tag{A.9}$$

$$R_w = \sqrt{\frac{\sum_{\boldsymbol{k}} w(\boldsymbol{k}) |I_{\mathrm{o}}(\boldsymbol{k}) - I_{\mathrm{c}}(\boldsymbol{k})|^2}{\sum_{\boldsymbol{k}} w(\boldsymbol{k}) |F_{\mathrm{o}}(\boldsymbol{k})|^2}} \tag{A.10}$$

$$S = \sqrt{\frac{\sum_{(\boldsymbol{k})} w(\boldsymbol{k}) |I_{\mathrm{o}}(\boldsymbol{k}) - I_{\mathrm{c}}(\boldsymbol{k})|^2}{N_k - N_{\mathrm{param}}}} \tag{A.11}$$

A.4.2 Rietveld analysis for powder diffraction

In principle, individual diffraction intensities cannot be extracted from powder diffraction patterns like single-crystal study because the diffraction is already one-dimensional, and multiple diffraction spots overlap in the peak. Moreover, the diffraction peaks from the sample cannot be distinguished without additional information when they coexist with some crystalline phases. Then, the diffraction profiles need to be examined by both profile shapes and structure models to reveal the detailed structure information including the atomic positions. The Rietveld analysis is a kind of whole pattern fitting analysis using various profile functions in addition to the structure models [220]. In this thesis, the Rietveld refinements were conducted using the *GSAS* software [141]. Then, each diffraction

peak can be calculated from structure factors and several factors as described in Appendix B. The peak intensities are distributed from the centre positions calculated from the structure models. Basically, the peak shapes of Bragg peaks are modelled by peak profile function with pseudo-Voigt description for convenience of calculation and reproducibility of spreading in Lorentz and Gaussian distributions for spectroscopic and statistical factors. The position-dependent peak broadening is modelled using several parameters. In the refinements for the data obtained at the BL11 of the MLF, J-PARC [136], TOF profile function 3 was selected [141]. The diffraction contribution to the observed diffraction profiles can be calculated by superposition of those from the sample and coexisting crystalline phases. The overall diffraction intensities are calculated as the sum of the diffraction contributions ad other intensities modelled by background functions. In this thesis, the shifted Chebyschev polynomial [221] was used.

The parameters of structure models and the functions are refined to minimise the function, M_p (Equation A.12), with weight, w, derived from error propagation. Here, the summation is for the whole profile region in time-of-flight for powder TOF diffraction. Some residual functions are used to investigate the quality of the least square refinements. R_p is simply derived from the observed and calculated intensities A.13. R_wp indicate the weighted residual A.14. χ^2 corresponds to the goodness of the least square refinement derived from the number of binns for observed intensities N_obs and refined parameters N_var.

$$M_\mathrm{p} = \sum w(I_\mathrm{o} - I_\mathrm{c})^2 \tag{A.12}$$

$$R_\mathrm{p} = \frac{\sum |I_\mathrm{o} - I_\mathrm{c}|}{\sum I_\mathrm{o}} \tag{A.13}$$

$$R_\mathrm{wp} = \sqrt{\frac{M_\mathrm{p}}{\sum w I_\mathrm{o}}} \tag{A.14}$$

$$\chi^2 = \frac{M_\mathrm{p}}{N_\mathrm{obs} - N_\mathrm{var}} \tag{A.15}$$

The Rietveld analysis is widely used for structure refinement, but some functions are not necessarily derived from physical explanation. Thus, it needs to care that the refinements strongly depends on the functions and models so that inappropriate ones lead to an artefact.

A.5 Structure factor $S(Q)$ from total scattering

Structure factors originally correspond to the Fourier transformation of distribution in real space without assumption of structural periodicity while crystal structure factor $F(\boldsymbol{k})$ represents the Fourier transformation of atomic distributions in the unit-cell as a representative average of periodic structure. Thus, structure factors can describe the non-periodic structural features with short-range order, such as local structure in non-crystalline materials like liquid and amorphous and disordered crystals.

However, diffractions from a non-periodic structure are neither sharp nor intense like Bragg peaks. The diffraction intensities cannot be extracted straightforwardly by simple peak fitting with the subtraction of background using arbitrary functions like the case of crystalline materials. The elastic scattering intensity $I(Q)$ can be measured experimentally after correction for attenuation, multiple scattering [139], and incoherent scattering [140]. Here, a one-dimensional function is sufficient because the orientational information is already lost in powder diffraction patterns. Then, the elastic scattering intensity, $I(Q)$, from the sample consisting of discrete atoms, i, with scattering length, b_i, can be described by the summation of orientationally averaged structure factor interferences as a function of the magnitude of the scattering vector, $Q = 4\pi \sin\theta/\lambda$ (Equation A.16). The terms can be separated into the interatomic and self terms (Equation (A.17)). The first term in Equation (A.17) corresponds to the coherent scattering intensity, $I_{\mathrm{coh}}(Q)$, and represents the interatomic structure of the scatterer. Then, scattering factor $S(Q)$ can be defined as Equation (A.18) in Faber-Ziman definition [222]. Here, the structure factor is normalised by the square of the average scattering length $\langle b \rangle$ of the sample and the number of atoms, N. The self-term, $\langle b^2 \rangle$, cancels out for uni-atomic system (*i.e.* $\langle b \rangle = b$).

$$
\begin{aligned}
I(Q) &= \left\langle \sum_i \sum_j b_i b_j \exp\{-2\pi i \boldsymbol{k} \cdot \boldsymbol{r}_{ij}\} \right\rangle_{\text{orientation}} \\
&= \sum_{i,j} b_i b_j \frac{\sin(Qr_{ij})}{Qr_{ij}} && \text{(A.16)} \\
&= \sum_{i \neq j} b_i b_j \frac{\sin(Qr_{ij})}{Qr_{ij}} + \sum_i b_i^2 && \text{(A.17)} \\
S(Q) - 1 &= \frac{I_{\mathrm{coh}}(Q)}{N\langle b \rangle^2} \\
&= \frac{I(Q)/N - \langle b^2 \rangle}{\langle b \rangle^2} && \text{(A.18)} \\
\langle b \rangle &= \sum^N c_X b_X \quad \langle b^2 \rangle = \sum^N c_X b_X^2
\end{aligned}
$$

A.5.1 Correlation functions for multi-atomic system

The structure factors $S(Q)$ derived from the experimental diffraction patterns contain multiple types of atomic pairs: *e.g.* the correlation functions derived in Chapter 3 is the mean function for pairs of O-D, O-O, D-D. The elastic scattering intensity is hence decomposed into the contribution of each atomic-pair correlation as a linear sum of each contribution to the intensity from the fraction c_X of the atomic species X (Equation (A.19)). Then structure factor $S(Q)$ can be rewritten using partial structure factor, $a_{XY}(Q)$, for pairs of atoms X and Y.

$$
\begin{aligned}
I(Q) &= \sum_{m,n}^{\text{atomic pair}} c_X c_Y b_X b_Y \sum_{i_X \neq j_Y} \frac{\sin(Qr_{i_X j_Y})}{Qr_{i_X j_Y}} + \sum_i b_i^2 && \text{(A.19)} \\
S(Q) &= \sum_X \sum_Y \frac{c_X c_Y b_X b_Y}{\langle b \rangle^2} a_{XY}(Q) && \text{(A.20)} \\
a_{XY}(Q) - 1 &= \sum_{i_X \neq j_Y} \frac{\sin(Qr_{i_X j_Y})}{Qr_{i_X j_Y}} && \text{(A.21)}
\end{aligned}
$$

Accordingly, the atomic pair distribution functions $g(r)$ can be decomposed into partial atomic pair distribution functions $g_{XY}(r)$.

$$g_{XY}(r) = 1 + \frac{1}{2\pi^2\rho_0 r}\int_0^\infty Q[S_{XY}(Q) - 1]\sin(Qr)dQ \tag{A.22}$$

A.5.2 Coordination number

Coordination numbers can be estimated for integrated area of radial distribution function (RDF) $N(r)$ derived from $g(r)$ (Equation (A.23)). $N(r)$ increase according to the interatomic distances with fluctuation from the asymptote of $4\pi r^2\rho_0$ derived as uniform spherical distribution with the average density of ρ_0. For a multi-atomic system, $N(r)$ is the average of partial interatomic correlations. Thus, the coordination number CN_{XY} from atom X for individual peak assignable to atom pairs X and Y can be derived by Equation A.24.

$$N(r) = 4\pi r^2\rho_0 g(r) \tag{A.23}$$

$$\begin{aligned} CN_{XY} &= c_X \cdot \frac{\langle b\rangle^2}{m_{XY}c_X c_Y b_X b_Y}\int_{r_{\mathrm{peak}}} N(r) \\ &= \frac{\langle b\rangle^2}{m_{XY}c_Y b_X b_Y}\int_{r_{\mathrm{peak}}} N(r) \end{aligned} \tag{A.24}$$

$$m_{XY} = \begin{cases} 1 & (X = Y) \\ 2 & (X \neq Y) \end{cases}$$

C $MgCl_2$ hydrates under high pressure

Acknowledgements

First of all, I would like to express my deepest gratitude to Prof. H. Kagi and Assoc. Prof. K. Komatsu for their continuous educational guidance, discussions, and encouragement. I am deeply grateful to Prof. S. Klotz for his help in the experiments and paper writing. Combinational studies with them broadened my scope for further research activities.

I appreciate Dr. T. Hattori (JAEA), Dr. T. Ohhara (JAEA), Dr. K. Munakata (CROSS), Dr. J. Abe (CROSS), and Dr. S. Machida (CROSS) for their devoted technical support to my experiments on powder and single-crystal neutron diffraction at the BL11 (PLANET) and the BL18 (SENJU) of the Materials and Life Science Experimental Facility (MLF) of the J-PARC. I wish to express thanks to Dr. M.T. Fernández-Díaz and Dr. O. Fabelo for their helpful assistance for neutron experiments at Institut Laue-Langevin (ILL). I am also grateful to all technical staffs at J-PARC and ILL for their support to the experiments.

Prof. T. Irifune and Dr. T. Shinmei (GRC, Ehime Univ.) and Prof. K. Sugiyama and Dr. Y. Kawamata (IMR, Tohoku Univ.) for their contributions in the synthesis of NPD and Zr-BMG, essential materials in the developed DAC in my thesis. I appreciate Dr. A. Kurio, (SYNTEK co.), Mr. S. Otsuka and Mr. T. Shimozawa (the science department of the University of Tokyo) for their significant contribution on the technical development in my thesis. They helped me again and again with their very quick and precise machining and constructive advice on the improvements

I am grateful to Prof. T. Yagi, Dr. K. Aoki, and Dr. Riko Oku-Iizuka for their advice for modifications of high-pressure cell assembly especially about the Bridgman type high-pressure cell. I also appreciate Dr. R. Yamane, Dr. K. Fukuyama, Mr. K. Nakayama, and Mr. H. Ito for their continuous discussions and encouragement. I thank all my colleagues in Kagi and Hirata groups.

I also appreciate the MERIT program for providing financial support and the opportunity to dedicate myself to the research activities. The collaboration to synthesise the Zr-BMG components was supported by the GIMRT program of the Institute for Materials Research, Tohoku University (Proposal No. 20K0085). Neutron diffraction experiments were performed through the J-PARC user programs (Nos. 2019B0116, 2020A152, 2020B0139, 2020B0156) and the ILL user programs (No. 5-15-624). Schematic images of crystal structures were described using the *VESTA* software [225].

Finally, I would also like to express my deepest gratitude to my family. Throughout my very long student life, they always supported and encouraged me.

References

1. Benedict, W. S., Gailar, N. & Plyler, E. K. Rotation-vibration spectra of deuterated water vapor. *J. Chem. Phys.* **24,** 1139–1165 (1956).
2. Clough, S. A. *et al.* Dipole moment of water from Stark measurements of H_2O, HDO, and D_2O. *J. Chem. Phys.* **2254,** 2254–2259 (1973).
3. Milovanović, M. R. *et al.* How flexible is the water molecule structure? Analysis of crystal structures and the potential energy surface. *Phys. Chem. Chem. Phys.* **22,** 4138–4143 (2020).
4. Elgabarty, H., Khaliullin, R. Z. & Kühne, T. D. Covalency of hydrogen bonds in liquid water can be probed by proton nuclear magnetic resonance experiments. *Nat. Commun.* **6,** 1–6 (2015).
5. Wang, B. *et al.* Electronic delocalization in small water rings. *Phys. Chem. Chem. Phys.* **17,** 2987–2990 (2015).
6. Wang, B. *et al.* Correlation between electron delocalization and structural planarization in small water rings. *Int. J. Quantum Chem.* **115,** 817–819 (2015).
7. Wang, B. *et al.* Molecular orbital analysis of the hydrogen bonded water dimer. *Sci. Rep.* **6,** 1–7 (2016).
8. Powles, J. G. The structure of the water molecule in liquid water. *Mol. Phys.* **42,** 757–765 (1981).
9. Zeidler, A. *et al.* Isotope effects in water as investigated by neutron diffraction and path integral molecular dynamics. *J. Phys. Condens. Matter* **24** (2012).
10. Kuhs, W. F. & Lehmann, M. S. in *Water Sci. Rev. 2* 1–66 (Cambridge University Press, 1986).
11. Floriano, M. A. *et al.* Direct determination of the intramolecular O-D distance in ice Ih and Ic by neutron diffraction. *Nature* **329,** 821–823 (1987).
12. Whalley, E. The O–H distance in ice. *Mol. Phys.* **28,** 1105–1108 (1974).
13. Mishima, O. Polyamorphism in water. *Proc. Japan Acad. Ser. B Phys. Biol. Sci.* **86,** 165–175 (2010).
14. Tanaka, H. Liquid-liquid transition and polyamorphism. *J. Chem. Phys.* **153** (2020).
15. Bernal, J. D. & Fowler, R. H. A Theory of Water and Ionic Solution, with Particular Reference to Hydrogen and Hydroxyl Ions. *J. Chem. Phys.* **1,** 515–548 (1933).
16. König, H. Eine kubische Eismodifikation. *Zeitschrift für Krist. - Cryst. Mater.* **105,** 279–286 (1943).
17. Komatsu, K. *et al.* Ice I_c without stacking disorder by evacuating hydrogen from hydrogen hydrate. *Nat. Commun.* **11,** 2–4 (2020).
18. Del Rosso, L. *et al.* Cubic ice Ic without stacking defects obtained from ice XVII. *Nat. Mater.* **19,** 663–668 (2020).
19. Malkin, T. L. *et al.* Stacking disorder in ice I. *Phys. Chem. Chem. Phys.* **17,** 60–76 (2015).
20. Hansen, T. C., Sippel, C. & Kuhs, W. F. Approximations to the full description of stacking disorder in ice I for powder diffraction. *Zeitschrift fur Krist.* **230,** 75–86 (2015).
21. Amaya, A. J. *et al.* How Cubic Can Ice Be? *J. Phys. Chem. Lett.* **8,** 3216–3222 (2017).
22. Peterson, S. W. & Levy, H. A. A single-crystal neutron diffraction study of heavy ice. *Acta Crystallogr.* **10,** 70–76 (1957).
23. Tajima, Y., Matsuo, T. & Suga, H. Phase transition in KOH-doped hexagonal ice. *Nature* **299,** 810–812 (1982).
24. Salzmann, C. G. The Preparation and Structures of Hydrogen Ordered Phases of Ice. *Science (80-.).* **311,** 1758–1761 (2006).
25. Salzmann, C. G. *et al.* Ice XV: A new thermodynamically stable phase of ice. *Phys. Rev. Lett.* **103,** 1–4 (2009).

26. Salzmann, C. G. *et al.* Detailed crystallographic analysis of the ice VI to ice XV hydrogen ordering phase transition. *J. Chem. Phys.* **145** (2016).

27. Yamane, R. *et al.* Experimental evidence for the existence of a second partially-ordered phase of ice VI. *Nat. Commun.* **12,** 1129 (2021).

28. Gasser, T. M. *et al.* Structural characterization of ice XIX as the second polymorph related to ice VI. *Nat. Commun.* **12,** 1128 (2021).

29. Komatsu, K. *et al.* Partially ordered state of ice XV. *Sci. Rep.* **6,** 28920 (2016).

30. Yamane, R., Komatsu, K. & Kagi, H. Direct evidence of the proton-dynamics crossover in ice VII from high-pressure dielectric measurements beyond 10 GPa. *Phys. Rev. B* **104,** 214304 (2021).

31. Wilson, H. F., Wong, M. L. & Militzer, B. Superionic to superionic phase change in water: Consequences for the interiors of uranus and neptune. *Phys. Rev. Lett.* **110,** 10–14 (2013).

32. Millot, M. *et al.* Nanosecond X-ray diffraction of shock-compressed superionic water ice. *Nature* **569,** 251–255 (2019).

33. Prakapenka, V. B. *et al.* Structure and properties of two superionic ice phases. *Nat. Phys.* **17,** 1233–1238 (2021).

34. Whalley, E., Davidson, D. W. & Heath, J. B. R. Dielectric Properties of Ice VII. Ice VIII: A New Phase of Ice. *J. Chem. Phys.* **45,** 3976–3982 (1966).

35. Johari, G. P., Lavergne, A. & Whalley, E. Dielectric properties of ice VII and VIII and the phase boundary between ice VI and VII. *J. Chem. Phys.* **61,** 4301–4306 (1974).

36. Jorgensen, J. D. *et al.* Structure of D_2O ice VIII from in situ powder neutron diffraction. *J. Chem. Phys.* **81,** 3211–3214 (1984).

37. Kuhs, W. F. *et al.* Structure and hydrogen ordering in ices VI, VII, and VIII by neutron powder diffraction. *J. Chem. Phys.* **81,** 3612–3623 (1984).

38. Polian, A. & Grimsditch, M. New high-pressure phase of H_2O: Ice X. *Phys. Rev. Lett.* **52,** 1312–1314 (1984).

39. Lee, C. *et al.* Ab initio studies on high pressure phases of ice. *Phys. Rev. Lett.* **69,** 462–465 (1992).

40. Pruzan, P., Chervin, J. C. & Canny, B. Stability domain of the ice VIII proton-ordered phase at very high pressure and low temperature. *J. Chem. Phys.* **99,** 9842–9846 (1993).

41. Goncharov, A. F. *et al.* Compression of ice to 210 gigapascals: Infrared evidence for a symmetric hydrogen-bonded phase. *Science (80-.).* **273,** 218–220 (1996).

42. Pruzan, P. *et al.* Raman Scattering and X-ray Diffraction of Ice in the Megabar Range. Occurrence of a Symmetric Disordered Solid above 62 GPa. *J. Phys. Chem. B* **101,** 6230–6233 (2002).

43. Aoki, K. *et al.* Infrared absorption study of the hydrogen-bond symmetrization in ice to 110 GPa. *Phys. Rev. B* **54,** 15673–15677 (1996).

44. Hemley, R. J., Chen, L. C. & Mao, H.-k. New transformations between crystalline and amorphous ice. *Nature* **338,** 638–640 (1989).

45. Klotz, S. *et al.* Recrystallisation of HDA ice under pressure by in-situ neutron diffraction to 3.9 GPa. *Zeitschrift fur Krist.* **218,** 117–122 (2003).

46. Takii, Y., Koga, K. & Tanaka, H. A plastic phase of water from computer simulation. *J. Chem. Phys.* **128,** 204501 (2008).

47. Aragones, J. L. & Vega, C. Plastic crystal phases of simple water models. *J. Chem. Phys.* **130,** 244504 (2009).

48. Aragones, J. L. *et al.* The phase diagram of water at high pressures as obtained by computer simulations of the TIP4P/2005 model: the appearance of a plastic crystal phase. *Phys. Chem. Chem. Phys.* **11,** 543–555 (2009).

49. Himoto, K., Matsumoto, M. & Tanaka, H. Lattice- and network-structure in plastic ice. *Phys. Chem. Chem. Phys.* **13,** 19876–19881 (2011).

50. Hernandez, J.-a. & Caracas, R. Proton dynamics and the phase diagram of dense water ice. *J. Chem. Phys.* **148,** 214501 (2018).

51. Goldman, N. *et al.* Bonding in the superionic phase of water. *Phys. Rev. Lett.* **94** (2005).

52. Goncharov, A. F. *et al.* Dynamic ionization of water under extreme conditions. *Phys. Rev. Lett.* **94** (2005).

53. Queyroux, J. A. *et al.* Melting Curve and Isostructural Solid Transition in Superionic Ice. *Phys. Rev. Lett.* **125,** 1–6 (2020).

54. Pruzan, P., Chervin, J. C. & Gauthier, M. Raman Spectroscopy Investigation of Ice VII and Deuterated Ice VII to 40 GPa. Disorder in Ice VII. *Europhys. Lett.* **13,** 81–87 (1990).

55. Komatsu, K. *et al.* Anomalous hydrogen dynamics of the ice VII-VIII transition revealed by high-pressure neutron diffraction. *Proc. Natl. Acad. Sci. U. S. A.* **117,** 6356–6361 (2020).

56. Iitaka, T. Simulating proton dynamics in high-pressure ice. *Rev. High Press. Sci. Technol. No Kagaku To Gijutsu* **23,** 124–132 (2013).

57. Kamb, B. & Davis, B. L. ICE VII, THE DENSEST FORM OF ICE. *Proc. Natl. Acad. Sci. U. S. A.* **52,** 1433–9 (1964).

58. Jorgensen, J. D. & Worlton, T. G. Disordered structure of D_2O ice VII from in situ neutron powder diffraction. *J. Chem. Phys.* **83,** 329–333 (1985).

59. Postberg, F. *et al.* Sodium salts in E-ring ice grains from an ocean below the surface of Enceladus. *Nature* **459,** 1098–1101 (2009).

60. Postberg, F. *et al.* A salt-water reservoir as the source of a compositionally stratified plume on Enceladus. *Nature* **474,** 620–622 (2011).

61. Zimmer, C., Khurana, K. K. & Kivelson, M. G. Subsurface Oceans on Europa and Callisto: Constraints from Galileo Magnetometer Observations. *Icarus* **147,** 329–347 (2000).

62. Kivelson, M. G., Khurana, K. K. & Volwerk, M. The permanent and inductive magnetic moments of Ganymede. *Icarus* **157,** 507–522 (2002).

63. Saur, J. *et al.* The search for a subsurface ocean in Ganymede with Hubble Space Telescope observations of its auroral ovals. *J. Geophys. Res. Sp. Phys.* **120,** 1715–1737 (2015).

64. Frank, M. R. *et al.* Experimental study of the NaCl–H_2O system up to 28GPa: Implications for ice-rich planetary bodies. *Phys. Earth Planet. Inter.* **155,** 152–162 (2006).

65. Klotz, S. *et al.* The preparation and structure of salty ice VII under pressure. *Nat. Mater.* **8,** 405–409 (2009).

66. Tschauner, O. *et al.* Ice-VII inclusions in diamonds: Evidence for aqueous fluid in Earth's deep mantle. *Science (80-.).* **359,** 1136–1139 (2018).

67. Journaux, B. *et al.* Salt partitioning between water and high-pressure ices. Implication for the dynamics and habitability of icy moons and water-rich planetary bodies. *Earth Planet. Sci. Lett.* **463,** 36–47 (2017).

68. Sears, V. F. Neutron scattering lengths and cross sections. *Neutron News* **3,** 26–37 (1992).

69. Boehler, R. *et al.* Large-volume diamond cells for neutron diffraction above 90 GPa. *High Press. Res.* **33,** 546–554 (2013).

70. Komatsu, K. *et al.* Developments of nano-polycrystalline diamond anvil cells for neutron diffraction experiments. *High Press. Res.* **40,** 184–193 (2020).

71. Akahama, Y. & Kawamura, H. Pressure calibration of diamond anvil Raman gauge to 410 GPa. *J. Phys. Conf. Ser.* **215** (2010).

72. Dubrovinsky, L. S. *et al.* Implementation of micro-ball nanodiamond anvils for high-pressure studies above 6 Mbar. *Nat. Commun.* **3,** 1163–1167 (2012).

73. Dubrovinsky, L. *et al.* The most incompressible metal osmium at static pressures above 750 gigapascals. *Nature* **525,** 226–229 (2015).

74. Dubrovinskaia, N. *et al.* Terapascal static pressure generation with ultrahigh yield strength nanodiamond. *Sci. Adv.* **2** (2016).

75. Sakai, T. *et al.* High-pressure generation using double stage micro-paired diamond anvils shaped by focused ion beam. *Rev. Sci. Instrum.* **86** (2015).

76. Yagi, T. *et al.* Review: high pressure generation techniques beyond the limit of conventional diamond anvils. *High Press. Res.* **40,** 148–161 (2020).

77. *International Tables for Crystallography* (ed Prince, E.) (International Union of Crystallography, Chester, England, 2006).

78. Doyle, P. A. & Turner, P. S. Relativistic Hartree–Fock X-ray and electron scattering factors. *Acta Crystallogr. Sect. A* **24,** 390–397 (1968).

79. Komatsu, K. *et al.* Development of a new P-T controlling system for neutron-scattering experiments. *High Press. Res.* **33,** 208–213 (2013).

80. Klotz, S., Hamel, G. & Frelat, J. A new type of compact large-capacity press for neutron and X-ray scattering. *High Press. Res.* **24,** 219–223 (2004).

81. Bull, C. L. *et al.* Time-of-flight single-crystal neutron diffraction to 10 GPa and above. *High Press. Res.* **29,** 780–791 (2009).

82. Bull, C. L. *et al.* High-pressure single-crystal neutron diffraction to 10 GPa by angle-dispersive techniques. *J. Appl. Crystallogr.* **44,** 831–838 (2011).

83. Bull, C. L. *et al.* Low-temperature neutron single-crystal diffraction studies of samples grown at high pressure. *High Press. Res.* **29,** 644–648 (2009).

84. Ridley, C. J., Jacobsen, M. K. & Kamenev, K. V. A finite-element study of sapphire anvils for increased sample volumes. *High Press. Res.* **35,** 148–161 (2015).

85. Kuhs, W. F. *et al.* In-situ crystal growth and neutron four-circle diffractometry under high pressure. *Phys. B Condens. Matter* **156-157,** 684–687 (1989).

86. Osakabe, T. *et al.* Pressure-induced antiferromagnetic order in filled skutterudite $PrFe_4P_{12}$ studied by single-crystal high-pressure neutron diffraction. *J. Phys. Soc. Japan* **79,** 4–10 (2010).

87. Okuchi, T. *et al.* Pulsed neutron powder diffraction at high pressure by a capacity-increased sapphire anvil cell. *High Press. Res.* **33,** 777–786 (2013).

88. Haberl, B. *et al.* Next-generation diamond cell and applications to single-crystal neutron diffraction. *Rev. Sci. Instrum.* **89,** 092902 (2018).

89. Massani, B. *et al.* On single-crystal neutron-diffraction in DACs: quantitative structure refinement of light elements on SNAP and TOPAZ. *High Press. Res.* **40,** 339–357 (2020).

90. Grzechnik, A., Meven, M. & Friese, K. Single-crystal neutron diffraction in diamond anvil cells with hot neutrons. *J. Appl. Crystallogr.* **51,** 351–356 (2018).

91. Boehler, R., Molaison, J. J. & Haberl, B. Novel diamond cells for neutron diffraction using multi-carat CVD anvils. *Rev. Sci. Instrum.* **88,** 083905 (2017).

92. Haberl, B. *et al.* Wide-angle diamond cell for neutron scattering. *High Press. Res.* **37,** 495–506 (2017).

93. Boehler, R. & De Hantsetters, K. New anvil designs in diamond-cells. *High Press. Res.* **24,** 391–396 (2004).

94. Grzechnik, A. *et al.* Combined X-ray and neutron single-crystal diffraction in diamond anvil cells. *J. Appl. Crystallogr.* **53,** 9–14 (2020).

95. Binns, J. *et al.* Use of a miniature diamond-anvil cell in high-pressure single-crystal neutron Laue diffraction. *IUCrJ* **3,** 168–179 (2016).

96. Merrill, L. & Bassett, W. A. Miniature diamond anvil pressure cell for single crystal x-ray diffraction studies. *Rev. Sci. Instrum.* **45,** 290–294 (1974).

97. Miletich, R., Allan, D. R. & Kuhs, W. F. High-Pressure Single-Crystal Techniques. *Rev. Mineral. Geochemistry* **41,** 445–519 (2000).

98. Moggach, S. A. *et al.* Incorporation of a new design of backing seat and anvil in a Merrill–Bassett diamond anvil cell. *J. Appl. Crystallogr.* **41,** 249–251 (2008).

99. Novelli, G. *et al.* Use of a miniature diamond-anvil cell in a joint X-ray and neutron high-pressure study on copper sulfate pentahydrate. *IUCrJ* **9,** 1–13 (2022).

100. Irifune, T. *et al.* Ultrahard polycrystalline diamond from graphite. *Nature* **421,** 599–600 (2003).

101. Sumiya, H. & Irifune, T. Hardness and deformation microstructures of nano-polycrystalline diamonds synthesized from various carbons under high pressure and high temperature. *J. Mater. Res.* **22,** 2345–2351 (2007).

102. Irifune, T., Isobe, F. & Shinmei, T. A novel large-volume Kawai-type apparatus and its application to the synthesis of sintered bodies of nano-polycrystalline diamond. *Phys. Earth Planet. Inter.* **228,** 255–261 (2014).

103. Loveday, J. S., McMahon, M. I. & Nelmes, R. J. The effect of diffraction by the diamonds of a diamond-anvil cell on single-crystal sample intensities. *J. Appl. Crystallogr.* **23,** 392–396 (1990).

104. Yokoyama, Y. *et al.* Tough Hypoeutectic Zr-Based Bulk Metallic Glasses. *Metall. Mater. Trans. A* **42,** 1468–1475 (2011).

105. Ichitsubo, T. *et al.* Microstructure of fragile metallic glasses inferred from ultrasound-accelerated crystallization in Pd-based metallic glasses. *Phys. Rev. Lett.* **95,** 1–4 (2005).

106. Komatsu, K. *et al.* A design of backing seat and gasket assembly in diamond anvil cell for accurate single crystal x-ray diffraction to 5 GPa. *Rev. Sci. Instrum.* **82,** 105107 (2011).

107. Komatsu, K. *et al.* Zr-based bulk metallic glass as a cylinder material for high pressure apparatuses. *High Press. Res.* **35,** 254–262 (2015).

108. Inoue, A. Stabilization of metallic supercooled liquid and bulk amorphous alloys. *Acta Mater.* **48,** 279–306 (2000).

109. Mao, H.-k. *et al.* Specific volume measurements of Cu, Mo, Pd, and Ag and calibration of the ruby R 1 fluorescence pressure gauge from 0.06 to 1 Mbar. *J. Appl. Phys.* **49,** 3276–3283 (1978).

110. Mao, H.-k., Xu, J. & Bell, P. M. Calibration of the ruby pressure gauge to 800 kbar under quasi-hydrostatic conditions. *J. Geophys. Res.* **91,** 4673 (1986).

111. Osakabe, T., Yamauchi, H. & Okuchi, T. Development of High-Pressure Technique for Single-Crystal Magnetic Neutron Diffraction under 10 GPa. *Rev. High Press. Sci. Technol.* **20,** 72–75 (2010).

112. Sidhu, S. S. *et al.* Neutron diffraction study of titanium-zirconium system. *J. Appl. Phys.* **27,** 1040–1042 (1956).

113. Klotz, S. *Techniques in High Pressure Neutron Scattering* (CRC Press, 2012).

114. Yokoyama, Y., Inoue, K. & Fukaura, K. Pseudo Float Melting State in Ladle Arc-Melt-Type Furnace for Preparing Crystalline Inclusion-Free Bulk Amorphous Alloy. *Mater. Trans.* **43,** 2316–2319 (2005).

115. Wiederhorn, S. M. Influence of Water Vapor on Crack Propagation in Soda-Lime Glass. *J. Am. Ceram. Soc.* **50,** 407–414 (1967).

116. Piermarini, G. J., Block, S. & Barnett, J. D. Hydrostatic limits in liquids and solids to 100 kbar. *J. Appl. Phys.* **44,** 5377–5382 (1973).

117. Klotz, S. *et al.* The effect of temperature on the hydrostatic limit of 4:1 methanol-ethanol under pressure. *High Press. Res.* **29,** 649–652 (2009).

118. Ohhara, T. *et al.* SENJU: A new time-of-flight single-crystal neutron diffractometer at J-PARC. *J. Appl. Crystallogr.* **49,** 120–127 (2016).

119. Sheldrick, G. M. Crystal structure refinement with *SHELXL*. *Acta Crystallogr. Sect. C Struct. Chem.* **71,** 3–8 (2015).

120. Ohhara, T. *et al.* Development of data processing software for a new TOF single crystal neutron diffractometer at J-PARC. *Nucl. Instruments Methods Phys. Res. Sect. A Accel. Spectrometers, Detect. Assoc. Equip.* **600,** 195–197 (2009).

121. Petříček, V., Dušek, M. & Palatinus, L. Crystallographic Computing System JANA2006: General features. *Zeitschrift für Krist. - Cryst. Mater.* **229,** 345–352 (2014).

122. Becker, P. J. & Coppens, P. Extinction within the limit of validity of the Darwin transfer equations. II. Refinement of extinction in spherical crystals of SrF_2 and LiF. *Acta Crystallogr. Sect. A* **30,** 148–153 (1974).

123. Kuhs, W. F. *et al.* Single crystal diffraction with X-rays and neutrons: High quality at high pressure? *High Press. Res.* **14,** 341–352 (1996).

124. Kamb, B. Structure of Ice VI. *Science (80-.).* **150,** 205–209 (1965).

125. Fortes, A. D., Knight, K. S. & Wood, I. G. Structure, thermal expansion and incompressibility of $MgSO_4{\cdot}9H_2O$, its relationship to meridianiite ($MgSO_4{\cdot}11H_2O$) and possible natural occurrences. *Acta Crystallogr. Sect. B Struct. Sci. Cryst. Eng. Mater.* **73,** 47–64 (2017).

126. Wang, W. *et al.* Investigation of high-pressure planetary ices by cryo-recovery. II. High-pressure apparatus, examples and a new high-pressure phase of $MgSO_4{\cdot}5H_2O$. *J. Appl. Crystallogr.* **51,** 692–705 (2018).

127. Yamashita, K. *et al.* Crystal structure of a high-pressure phase of magnesium chloride hexahydrate determined by in-situ X-ray and neutron diffraction methods. *Acta Crystallogr. Sect. C Struct. Chem.* **75,** 1605–1612 (2019).

128. Fabbiani, F. P. *et al.* Pressure-induced formation of a solvate of paracetamol. *Chem. Commun.,* 3004 (2003).

129. Fabbiani, F. P. *et al.* High-pressure recrystallisation—a route to new polymorphs and solvates. *CrystEngComm* **6,** 504–511 (2004).

130. Klotz, S. *et al.* Bulk moduli and equations of state of ice VII and ice VIII. *Phys. Rev. B* **95,** 174111 (2017).

131. Komatsu, K. *et al.* Crystal structure of magnesium dichloride decahydrate determined by X-ray and neutron diffraction under high pressure. *Acta Crystallogr. Sect. B Struct. Sci. Cryst. Eng. Mater.* **71,** 74–80 (2015).

132. Kuo, J.-L. & Klein, M. L. Structure of Ice-VII and Ice-VIII: A Quantum Mechanical Study. *J. Phys. Chem. B* **108,** 19634–19639 (2004).

133. Nelmes, R. J. *et al.* Multisite Disordered Structure of Ice VII to 20 GPa. *Phys. Rev. Lett.* **81,** 2719–2722 (1998).

134. Knight, C. & Singer, S. J. Site disorder in ice VII arising from hydrogen bond fluctuations. *J. Phys. Chem. A* **113,** 12433–12438 (2009).

135. Klotz, S. *et al.* Freezing of glycerol–water mixtures under pressure. *J. Phys. Condens. Matter* **24,** 325103 (2012).

136. Hattori, T. *et al.* Design and performance of high-pressure PLANET beamline at pulsed neutron source at J-PARC. *Nucl. Instruments Methods Phys. Res. Sect. A Accel. Spectrometers, Detect. Assoc. Equip.* **780,** 55–67 (2015).

137. Iizuka, R. *et al.* An opposed-anvil-type apparatus with an optical window and a wide-angle aperture for neutron diffraction. *High Press. Res.* **32,** 430–441 (2012).

138. Komatsu, K. *et al.* Performance of ceramic anvils for high pressure neutron scattering. *High Press. Res.* **34,** 494–499 (2014).

139. Blech, I. A. & Averbach, B. L. Multiple scattering of neutrons in vanadium and copper. *Phys. Rev.* **137,** 1–4 (1965).

140. Kameda, Y. *et al.* Inelasticity Effect on Neutron Scattering Intensities of the Null-H_2O. *J. Neutron Res.* **11,** 153–163 (2003).

141. Larson, A. C. & Von Dreele, R. B. GSAS manual. *Rep. LAUR* **86-748,** 285–287 (2004).

142. Sakata, M. & Takata, M. Electron density distribution by the maximum entropy method. *Nihon Kessho Gakkaishi* **32,** 175–183 (1990).

143. Sakata, M. *et al.* Maximum-entropy-method analysis of neutron diffraction data. *J. Appl. Crystallogr.* **26,** 159–165 (1993).

144. Momma, K. *et al.* Dysnomia, a computer program for maximum-entropy method (MEM) analysis and its performance in the MEM-based pattern fitting. *Powder Diffr.* **28,** 184–193 (2013).

145. Loubeyre, P. *et al.* Modulated phases and proton centring in ice observed by X-ray diffraction up to 170 GPa. *Nature* **397,** 503–506 (1999).

146. Somayazulu, M. *et al.* In situ high-pressure x-ray diffraction study of H_2O ice VII. *J. Chem. Phys.* **128,** 064510 (2008).

147. Kuhs, W. F. & Lehmann, M. S. The structure of ice Ih by neutron diffraction. *J. Phys. Chem.* **87,** 4312–4313 (1983).

148. Powles, J. G. Slow neutron scattering by molecules IV. Recoil corrections for diatomic molecules—time of flight. *Mol. Phys.* **36,** 1181–1198 (1978).

149. Zeidler, A. *et al.* Oxygen as a site specific probe of the structure of water and oxide materials. *Phys. Rev. Lett.* **107,** 1–5 (2011).

150. Umemoto, K. *et al.* Order–disorder phase boundary between ice VII and VIII obtained by first principles. *Chem. Phys. Lett.* **499,** 236–240 (2010).

151. Guthrie, M. *et al.* Structure and disorder in ice VII on the approach to hydrogen-bond symmetrization. *Phys. Rev. B* **99,** 184112 (2019).

152. Singer, S. J. *et al.* Hydrogen-bond topology and the ice VII/VIII and ice I*h*/XI proton-ordering phase transitions. *Phys. Rev. Lett.* **94,** 1–4 (2005).

153. Knight, C. *et al.* Hydrogen bond topology and the ice VII/VIII and Ih/XI proton ordering phase transitions. *Phys. Rev. E - Stat. Nonlinear, Soft Matter Phys.* **73,** 1–14 (2006).

154. Noguchi, N. & Okuchi, T. Self-diffusion of protons in H_2O ice VII at high pressures: Anomaly around 10 GPa. *J. Chem. Phys.* **144** (2016).

155. Hirata, M. *et al.* Phase Diagram of TIP4P/2005 Water at High Pressure. *Langmuir* **33,** 11561–11569 (2017).

156. Yagasaki, T., Matsumoto, M. & Tanaka, H. Phase Diagrams of TIP4P/2005, SPC/E, and TIP5P Water at High Pressure. *J. Phys. Chem. B* **122,** 7718–7725 (2018).

157. Bove, L. E. *et al.* Pressure-induced polyamorphism in salty water. *Phys. Rev. Lett.* **106,** 3–6 (2011).

158. Ludl, A.-A. *et al.* Structural characterization of eutectic aqueous NaCl solutions under variable temperature and pressure conditions. *Phys. Chem. Chem. Phys.* **17,** 14054–14063 (2015).

159. Klotz, S. *et al.* Ice VII from aqueous salt solutions: From a glass to a crystal with broken H-bonds. *Sci. Rep.* **6,** 32040 (2016).

160. Bove, L. E. *et al.* Effect of salt on the H-bond symmetrization in ice. *Proc. Natl. Acad. Sci.* **112,** 8216–8220 (2015).

161. Ludl, A.-A. *et al.* Probing ice VII crystallization from amorphous NaCl-D_2O solutions at gigapascal pressures. *Phys. Chem. Chem. Phys.* **19,** 1875–1883 (2017).

162. Watanabe, M. *et al.* Structural incorporation of $MgCl_2$ into ice VII at room temperature. *Jpn. J. Appl. Phys.* **56,** 05FB03 (2017).

163. Mishima, O., Calvert, L. D. & Whalley, E. 'Melting ice' I at 77 K and 10 kbar: a new method of making amorphous solids. *Nature* **310,** 393–395 (1984).

164. Mishima, O., Ld, C. & E, W. An Apparently 1st-Order Transition Between 2 Amorphous Phases Of Ice Induced By Pressure. *Nature* **314,** 76–78 (1985).

165. Poole, P. H. *et al.* Phase behaviour of metastable water. *Nature* **360,** 324–328 (1992).

166. Mishima, O. Liquid-liquid critical point in heavy water. *Phys. Rev. Lett.* **85,** 334–336 (2000).

167. Koza, M. *et al.* Formation of ice XII at different conditions. *Nature* **397,** 660–661 (1999).

168. Klotz, S. *et al.* Structure of High-Density Amorphous Ice under Pressure. *Phys. Rev. Lett.* **89,** 285502 (2002).

169. Nelmes, R. J. *et al.* Annealed high-density amorphous ice under pressure. *Nat. Phys.* **2,** 414–418 (2006).

170. Strässle, T. *et al.* Temperature dependence of the pressure-induced amorphization of ice I h studied by high-pressure neutron diffraction to 30 K. *Phys. Rev. B - Condens. Matter Mater. Phys.* **82,** 80–83 (2010).

171. Stern, J. N., Seidl-Nigsch, M. & Loerting, T. Evidence for high-density liquid water between 0.1 and 0.3 GPa near 150 K. *Proc. Natl. Acad. Sci. U. S. A.* **116,** 9191–9196 (2019).

172. Foffi, R. & Sciortino, F. Structure of High-Pressure Supercooled and Glassy Water. *Phys. Rev. Lett.* **127,** 175502 (2021).

173. Frank, M. R. *et al.* Temperature induced immiscibility in the NaCl–H_2O system at high pressure. *Phys. Earth Planet. Inter.* **170,** 107–114 (2008).

174. Frank, M. R. *et al.* A comparison of ice VII formed in the H_2O, NaCl–H_2O, and CH_3OH–H2O systems: Implications for H_2O-rich planets. *Phys. Earth Planet. Inter.* **215,** 12–20 (2013).

175. Frank, M. R. *et al.* Potassium chloride-bearing ice VII and ice planet dynamics. *Geochim. Cosmochim. Acta* **174,** 156–166 (2016).

176. Zeng, Q. *et al.* Compression icing of room-temperature NaX solutions (X = F, Cl, Br, I). *Phys. Chem. Chem. Phys.* **18,** 14046–14054 (2016).

177. Zeng, Q. *et al.* Room-temperature NaI/H_2O compression icing: Solute-solute interactions. *Phys. Chem. Chem. Phys.* **19,** 26645–26650 (2017).

178. Bronstein, Y. *et al.* Quantum versus classical protons in pure and salty ice under pressure. *Phys. Rev. B* **93,** 1–5 (2016).

179. Salzmann, C. G. *et al.* Ammonium Fluoride as a Hydrogen-Disordering Agent for Ice. *J. Phys. Chem. C* **123,** 16486–16492 (2019).

180. Elarby-Aouizerat, A. *et al.* Metastable crystallization products and metastable phase diagram of the glassy and supercooled aqueous ionic solutions of LiCl. *J. Non. Cryst. Solids* **104,** 203–210 (1988).

181. Angell, C. A. & Sare, E. J. Glass-forming composition regions and glass transition temperatures for aqueous electrolyte solutions. *J. Chem. Phys.* **52,** 1058–1068 (1970).

182. Prével, B. *et al.* Medium and long range correlations in the electrolyte LiCl·4H_2O: Transition to the glass regime. *J. Chem. Phys.* **103,** 1897–1903 (1995).

183. Prével, B. *et al.* Structural characterization of an electrolytic aqueous solution, LiCl·6H_2O, in the glass, supercooled liquid, and liquid states. *J. Chem. Phys.* **103,** 1886–1896 (1995).

184. Maurin, P. O. α and β process in the glass forming electrolyte solution LiCl-6H_2O. *J. Chem. Phys.* **109,** 10936–10939 (1998).

185. Suzuki, Y. & Mishima, O. Two distinct Raman profiles of glassy dilute LiCl solution. *Phys. Rev. Lett.* **85,** 1322–1325 (2000).

186. Mishima, O. Application of polyamorphism in water to spontaneous crystallization of emulsified LiCl-H_2O solution. *J. Chem. Phys.* **123,** 154506 (2005).

187. Mishima, O. Phase separation in dilute LiCl–H_2O solution related to the polyamorphism of liquid water. *J. Chem. Phys.* **126,** 244507 (2007).

188. Suzuki, Y. & Mishima, O. Differences between pressure-induced densification of LiCl-H_2O glass and polyamorphic transition of H_2O. *J. Phys. Condens. Matter* **21** (2009).

189. Suzuki, Y. & Mishima, O. Sudden switchover between the polyamorphic phase separation and the glass-to-liquid transition in glassy LiCl aqueous solutions. *J. Chem. Phys.* **138** (2013).

190. Lyashchenko, A. K. & Malenkov, G. G. X-ray investigation of ammonium fluoride-ice systems. *J. Struct. Chem.* **10,** 616–617 (1970).

191. Brill, R. & ZAROMB, S. Mixed Crystals of Ice and Ammonium Fluoride. *Nature* **173,** 316–317 (1954).

192. Zaromb, S. & Brill, R. Solid solutions of ice and NH_4F and their dielectric properties. *J. Chem. Phys.* **24,** 895–902 (1956).

193. Labowitz, L. C. & Westrum, E. F. A THERMODYNAMIC STUDY OF THE SYSTEM AMMONIUM FLUORIDE-WATER. II. THE SOLID SOLUTION OF AMMONIUM FLUORIDE IN ICE. *J. Phys. Chem.* **65,** 408–414 (1961).

194. Shin, K. *et al.* Crystal engineering the clathrate hydrate lattice with NH_4F. *CrystEngComm* **16,** 7209–7217 (2014).

195. Park, S. *et al.* Incorporation of ammonium fluoride into clathrate hydrate lattices and its significance in inhibiting hydrate formation. *Chem. Commun.* **51,** 8761–8764 (2015).

196. Shephard, J. J. *et al.* Doping-induced disappearance of ice II from water's phase diagram. *Nat. Phys.* **14,** 569–572 (2018).

197. Fan, X. *et al.* Predicting the hydrogen bond ordered structures of ice Ih, II, III, VI and ice VII: DFT methods with localized based set. *Comput. Mater. Sci.* **49,** S170–S175 (2010).

198. Nakamura, T. *et al.* Thermodynamic Stability of Ice II and Its Hydrogen-Disordered Counterpart: Role of Zero-Point Energy. *J. Phys. Chem. B* **120,** 1843–1848 (2016).

199. Sharif, Z. *et al.* Effect of ammonium fluoride doping on the ice III to ice IX phase transition. *J. Chem. Phys.* **154** (2021).

200. La Placa, S. J. *et al.* On a nearly proton-ordered structure for ice IX. *J. Chem. Phys.* **58,** 567–580 (1973).

201. Londono, J. D., Kuhs, W. F. & Finney, J. L. Neutron diffraction studies of ices III and IX on under-pressure and recovered samples. *J. Chem. Phys.* **98,** 4878–4888 (1993).

202. Strässle, T. *et al.* Equation of state of lead from high-pressure neutron diffraction up to 8.9 GPa and its implication for the NaCl pressure scale. *Phys. Rev. B - Condens. Matter Mater. Phys.* **90,** 1–8 (2014).

203. MacFarlane, D. R., Kadiyala, R. K. & Angell, C. A. Homogeneous nucleation and growth of ice from solutions. TTT curves, the nucleation rate, and the stable glass criterion. *J. Chem. Phys.* **79,** 3921–3927 (1983).

204. MacFarlane, D. R., Kadiyala, R. K. & Angell, C. A. Direct observation of time-temperature-transformation curves for crystallization of ice from solutions by a homogeneous mechanism. *J. Phys. Chem.* **87,** 1094–1095 (1983).

205. Suzuki, Y. & Mishima, O. Raman spectroscopic study of glassy water in dilute lithium chloride aqueous solution vitrified under pressure. *J. Chem. Phys.* **117,** 1673–1676 (2002).

206. SETO, Y. *et al.* Development of a Software Suite on X-ray Diffraction Experiments. *Rev. High Press. Sci. Technol.* **20,** 269–276 (2010).

207. Salzmann, C. G. *et al.* Pure ice IV from high-density amorphous ice. *J. Phys. Chem. B* **106,** 5587–5590 (2002).

208. Salzmann, C. G., Mayer, E. & Hallbrucker, A. Effect of heating rate and pressure on the crystallization kinetics of high-density amorphous ice on isobaric heating between 0.2 and 1.9 GPa. *Phys. Chem. Chem. Phys.* **6,** 5156 (2004).

209. Ostwald, W. Studien über die Bildung und Umwandlung fester Körper. *Zeitschrift für Phys. Chemie* **22U,** 289–330 (1897).

210. Stranski, I. N. & Totomanow, D. Keimbildungsgeschwindigkeit und OSTWALDsche Stufenregel. *Zeitschrift für Phys. Chemie* **163A,** 399–408 (1933).

211. Ten Wolde, P. R. & Frenkel, D. Homogeneous nucleation and the Ostwald step rule. *Phys. Chem. Chem. Phys.* **1,** 2191–2196 (1999).

212. Shephard, J. J. *et al.* Is High-Density Amorphous Ice Simply a "Derailed" State along the Ice I to Ice IV Pathway? *J. Phys. Chem. Lett.* **8,** 1645–1650 (2017).

213. Bauer, R. *et al.* Slow compression of crystalline ice at low temperature. *Nature* **585,** E9–E10 (2020).

214. Sharif, Z. & Salzmann, C. G. Comparison of the phase transitions of high-pressure phases of ammonium fluoride and ice at ambient pressure. *J. Chem. Phys.* **156,** 014502 (2022).

215. Maekawa, F. *et al.* First neutron production utilizing J-PARC pulsed spallation neutron source JSNS and neutronic performance demonstrated. *Nucl. Instruments Methods Phys. Res. Sect. A Accel. Spectrometers, Detect. Assoc. Equip.* **620,** 159–165 (2010).

216. Stone, M. B. *et al.* A radial collimator for a time-of-flight neutron spectrometer. *Rev. Sci. Instrum.* **85** (2014).

217. Wright, A. F., Berneron, M. & Heathman, S. P. Radial collimator system for reducing background noise during neutron diffraction with area detectors. *Nucl. Instruments Methods* **180,** 655–658 (1981).

218. IUCr. *Core CIF dictionary Version2.4.5* 2014.

219. Wilson, A. J. Statistical bias in least-squares refinement. *Acta Crystallogr. Sect. A* **32,** 994–996 (1976).

220. Rietveld, H. M. A profile refinement method for nuclear and magnetic structures. *J. Appl. Crystallogr.* **2,** 65–71 (1969).

221. Abramowitz, M. & Stegun, I. A. *Handbook of Mathematical Functions: With Formulas, Graphs, and Mathematical Tables* (Dover Publications, 1965).

222. Faber, T. E. & Ziman, J. M. A theory of the electrical properties of liquid metals. *Philos. Mag.* **11,** 153–173 (1965).

223. Guthrie, M. *et al.* Radiation attenuation by single-crystal diamond windows. *J. Appl. Crystallogr.* **50,** 76–86 (2017).

224. Yamashita, K. *et al.* A nano-polycrystalline diamond anvil cell with bulk metallic glass cylinder for single-crystal neutron diffraction. *High Press. Res.* **40,** 88–95 (2020).

225. Momma, K. & Izumi, F. *VESTA 3* for three-dimensional visualization of crystal, volumetric and morphology data. *J. Appl. Crystallogr.* **44,** 1272–1276 (2011).